Air Force Institute of Technology

AFIT Scholar

3-14-2007

Assessment of the Impact of Various Ionospheric Models on High Frequency Signal Raytracing

Joshua T. Werner

Follow this and additional works at: https://scholar.afit.edu/etd

Part of the Atmospheric Sciences Commons

Recommended Citation

Werner, Joshua T., "Assessment of the Impact of Various Ionospheric Models on High Frequency Signal Raytracing" (2007). *Theses and Dissertations*. 2913.
https://scholar.afit.edu/etd/2913

www.manaraa.com

ASSESSMENT OF THE IMPACT OF VARIOUS IONOSPHERIC MODELS ON HIGH-FREQUENCY SIGNAL RAYTRACING

THESIS

Joshua T. Werner, First Lieutenant, USAF

AFIT/GAP/ENP/07-07

DEPARTMENT OF THE AIR FORCE
AIR UNIVERSITY

AIR FORCE INSTITUTE OF TECHNOLOGY

Wright-Patterson Air Force Base, Ohio

APPROVED FOR PUBLIC RELEASE; DISTRIBUTION UNLIMITED

The views expressed in this thesis are those of the author and do not reflect the official policy or position of the United States Air Force, Department of Defense, or the U.S. Government.

AFIT/GAP/ENP/07-07

ASSESSMENT OF THE IMPACT OF VARIOUS IONOSPHERIC MODELS
ON HIGH-FREQUENCY SIGNAL RAYTRACING

THESIS

Presented to the Faculty

Department of Engineering Physics

Graduate School of Engineering and Management

Air Force Institute of Technology

Air University

Air Education and Training Command

In Partial Fulfillment of the Requirements for the

Degree of Master of Science in Applied Physics

Joshua T. Werner, BS
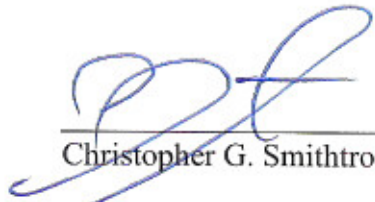
First Lieutenant, USAF

March 2007

APPROVED FOR PUBLIC RELEASE; DISTRIBUTION UNLIMITED

AFIT/GAP/ENP/07-07

ASSESSMENT OF THE IMPACT OF VARIOUS IONOSPHERIC MODELS
ON HIGH-FREQUENCY SIGNAL RAYTRACING
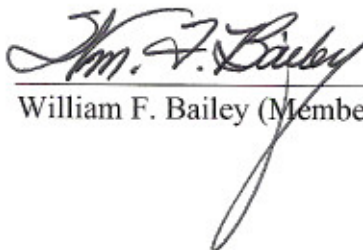
Joshua T. Werner, BS
First Lieutenant, USAF

Approved:

_____
Christopher G. Smithtro, PhD (Chairman)

13 Mar 07
Date

_____
William S. Borer (Member)

12 MAR 2007
Date

_____
William F. Bailey (Member)

14 Mar. '07
Date

Abstract

An assessment of the impact of various ionospheric models on high-frequency (HF) signal raytracing is presented. Ionospheric refraction can strongly affect the propagation of HF signals. Consequently, Department of Defense missions such as over-the-horizon RADAR, HF communications, and geo-location all depend on an accurate specification of the ionosphere. Five case studies explore ionospheric conditions ranging from quiet conditions to solar flares and geomagnetic storms. It is shown that an E layer by itself can increase an HF signal's ground range by over 100 km, stressing the importance of accurately specifying the lower ionosphere. It is also shown that the GPSII model has the potential to capture the expected daily variability of the ionosphere by using Total Electron Content data. This daily variability can change an HF signal's ground range by as much as 5 km per day. The upper-ionospheric response to both a solar flare and a geomagnetic storm is captured by the GPSII model. In contrast, the GPSII model does not capture the lower-ionospheric response to either event. These results suggest that using the GPSII model's passive technique by itself may only be beneficial to specifying the ionosphere above the E region, especially during solar flares and geomagnetic storms.

To My Family

and

To Space Exploration

Acknowledgments

I would like to express my sincere appreciation to my advisors for their leadership and guidance throughout the course of this thesis. A special thanks to Maj Chris Smithtro, your insight and experience was greatly appreciated. I would also like to thank Dr. William Borer at the Air Force Research Laboratory, for both the opportunity and latitude provided to me in this exploration. This daunting endeavor would never have progressed without the incredible assistance provided by Dr. Mark Hausman, Dr. L.J. Nickisch, Dr. Sergey Fridman, and 2Lt Curtis Baragona. Thank you all. Though I never verbalized my appreciation enough, the daily support and perfectly timed comic relief of my colleagues proved invaluable in maintaining my sanity. For that reason, I will never forget the camaraderie of Capt Brett Spangler, Capt Shaun Easley, and especially that of fellow weatherman throughout this entire adventure, SMSgt Rob Steenburgh.

To my family and friends … you know who you are. Your support and encouragement during this remarkable journey will never be forgotten. This is for you.

/signed/
Joshua Tye Werner

Table of Contents

List of Figures

List of Tables

ASSESSMENT OF THE IMPACT OF VARIOUS IONOSPHERIC MODELS

ON HIGH-FREQUENCY SIGNAL RAYTRACING

Introduction

Motivation

The ionosphere affects a wide array of current Department of Defense (DoD) missions. For example, the ability to communicate with satellites relies on electromagnetic signals successfully propagating through the ionosphere without excessive attenuation or refraction. Furthermore, high-frequency (HF) communications, over-the-horizon RADAR (OTHR), and certain methods of target direction finding all require electromagnetic signals to be refracted within the ionosphere. Future combat operations will continue to rely on our ability to precisely and accurately locate an enemy's position. Active sensing techniques can regrettably reveal the locations of friendly forces. This research focuses on the goal of developing an ability to geo-locate an enemy solely through intercepted communications. Even better, perform this geo-location passively without revealing the location of friendly forces. The future success of geo-location, as well as the other DoD missions, remains highly dependent on our ability to accurately measure and predict the dynamic state of the ionosphere.

One of the most recent advances in ionospheric modeling is the NorthWest Research Associates' (NWRA) Global Positioning System (GPS) Ionospheric Inversion (GPSII) model. As its name suggests, the model employs real-time Total Electron Content (TEC) information that is passively obtained from GPS signals. Two additional

1

ionospheric models currently available are the 2001 version of the International Reference Ionosphere (IRI-2001) model and the Parameterized Ionospheric Model (PIM). This thesis will focus on assessing the impact of these ionospheric models on HF signal raytracing when applied to the critical national defense mission of geo-location.

For the purpose of this thesis, geo-location describes the act of locating and/or tracking an enemy using HF signals. The two main techniques of geo-location use either multiple receiver sites or a single receiver site. This thesis focuses on a rigorous version of the latter technique, commonly referred to as "single site location" (SSL), which uses a complex three-dimensional raytracing algorithm and an ionospheric model to predict a signal's propagation path.

Ionospheric refraction can greatly affect the propagation behavior of a signal, especially in the HF range of frequencies. If the state of the ionosphere is not properly specified, the raytracing algorithm will produce an erroneous enemy location. The primary objective of this thesis is to assess the impact of the three ionospheric models on HF signal raytracing during various ionospheric conditions. The secondary objective is to determine whether using passive techniques to model the ionosphere is sufficiently accurate for geo-location. Categorizing the models' strengths and weaknesses will improve our ability to locate an enemy and, in turn, enhance the first four stages of the Air Force's six-stage "kill chain", which is find, fix, track, and target.

Overview

This thesis includes a comparison of high-frequency (HF) signal raytracing using the 2001 version of the International Reference Ionosphere (IRI-2001) model, the Parameterized Ionospheric Model (PIM), and the new Global Positioning System (GPS)

2

Ionospheric Inversion (GPSII) model. These comparisons are done for various ionospheric conditions, including: quiet, daily variability, solar flare, and geomagnetic storming. Model strengths and weaknesses are discussed, as well as whether using passive techniques to model the ionosphere is sufficiently accurate for geo-location.

Chapter two describes important background knowledge: the ionospheric environment (structure and behavior), signal propagation, ionospheric models, geo-location, and raytracing. Chapter three discusses the methodology used for this thesis, which is mostly the procedures for properly integrating the three main components of data collection, processing, and visualization: the ionospheric model, raytracing algorithm, and MATLAB® software. Chapter four presents the case study results, while chapter five provides conclusions and recommendations for future research.

Results Preview

The case studies reveal many interesting characteristics of the ionospheric models when applied to HF signal raytracing. It is shown that the ionosphere's E layer by itself can increase a signal's ground range by over 100 km, stressing the importance of accurately specifying the lower ionosphere. It is also shown that the GPSII model has the potential to capture the expected daily variability of the ionosphere by using TEC data, which can affect a signal's ground range by as much as 5 km per day. Furthermore, the GPSII model can capture the upper-ionospheric response to both a solar flare and a geomagnetic storm, yet cannot capture the lower-ionospheric response to either event. These results suggest that using the GPSII model's passive technique by itself may only be beneficial to specifying the ionosphere above the E region, especially during solar flares and geomagnetic storms.

3

Background

Ionospheric Environment

The ionosphere is defined as the ionized region of the Earth's upper atmosphere, comprised of several layers containing free electrons and various ionized particles. Solar photons provide the primary source of ionization, as extreme ultraviolet (EUV) and x-ray radiation break apart neutral atmospheric molecules to produce ions and free electrons. Secondary sources of ionization are photoelectrons, energetic particle precipitation, auroral precipitation, scattered radiation, starlight, and meteors. The mid-latitude ionosphere, in which this thesis will focus, is composed of the following layers: D, E, F_1, F_2, and the topside ionosphere. It is typically accepted that the ionosphere begins at around 60 kilometers (km) and extends to approximately 1000 km, depending on the degree of solar activity. The ionosphere transitions to the plasmasphere above 1000 km. *Davies* [1989] provides a good illustration of the ionospheric regions, reproduced in Figure 1. Each layer can be distinguished by a local peak in the electron density profile corresponding to a particular dominating ion species. In addition, each layer is controlled by different production and loss mechanisms with varying reaction rates. The remainder of this section will briefly describe each layer and their relevant temporal behavior.

The D region (60 to 90 km) is dominated by photochemical processes and has the most diverse composition, including: molecular ions, positive and negative ions, and water cluster ions. Consequently, this region is considered to be the most difficult to model and observe with any reliability [*Schunk and Nagy*, 2000]. The E region (90 to 150 km) is also dominated by photochemistry and consists primarily of molecular ions such as O_2^+, N_2^+, and NO^+ that form an observable peak in the density profile. The F_1

4

region (150 to 250 km) is still dominated by photochemical processes, yet is the transition region in which O^+ becomes the principal ion species. Although not dominant, there are also transport mechanisms present in this region, such as ambipolar diffusion, wind-induced drifts along magnetic field lines, and electrodynamic drifts across magnetic field lines [*Schunk and Nagy*, 2000]. The F_2 region (250 to 450 km) is where the importance of these transport mechanisms become balanced with the photochemical processes, creating a well-defined peak in the O^+ density profile. The topside ionosphere is the region above the F_2 peak where the transport mechanisms dominate, resulting in an exponential decrease in O^+ density with altitude. Given that this thesis focuses on geo-location, we are only interested in the ionosphere's behavior below the F_2 peak where maximum refraction of HF signals occurs.
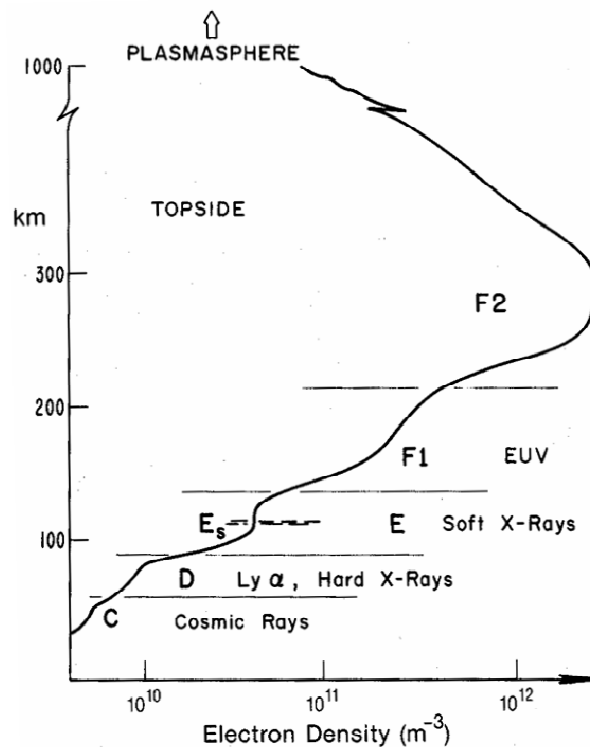
Figure 1: Ionosphere electron density (m^{-3}) as a function of altitude (km) depicting the typical ionospheric layers observed on a mid-latitude summer day. The main bands of solar and cosmic ionizing radiation are noted [*Davies*, 1989].

5

One of the main techniques for obtaining real-time observations of the ionosphere below the F2 peak uses vertical incidence ionosondes, which are HF radars that are directed toward zenith. A sweep of frequencies is transmitted and the time delay of each signal's return is measured. The following expression relates the plasma frequency f_p of a layer (in MHz) to the electron density N_e (in m^{-3}) [*Sturrock*, 1994].

$$f_p\left(\text{MHz}\right) \simeq 9 \times 10^{-6}\sqrt{N_e(\text{m}^{-3})} \tag{1}$$

Ignoring the effect of the Earth's magnetic field, the critical frequency f_c of the ionosphere is the maximum frequency that can be still be refracted back to the ground when transmitted toward zenith. Signals with frequencies higher than the critical frequency will pass through the ionosphere. A signal's "virtual height of reflection" is equivalent to the distance that the signal would have traveled during half the elapsed travel time, assuming it traveled at the speed of light in free space. An ionogram is a plot of this virtual height as a function of frequency; an example is shown in Figure 2. In this figure, the solid black line is the plasma frequency (which equates to electron density via Equation 1) as a function of height, found by inverting the observed virtual height. Note that ionosondes can only determine the "bottomside" frequency profile of the ionosphere; models are used to estimate the "topside" profile. Estimates of the electron density can be used to determine the ionosphere's refractive index as a function of position, which is needed for raytracing.

The mid-latitude ionosphere exhibits dramatic changes on many timescales, including diurnal, seasonal, solar cycle, and irregular variations. A good example of the diurnal variation is seen in Figure 3, where the plasma frequency ($f_p \propto \sqrt{N_e}$) is shown

6
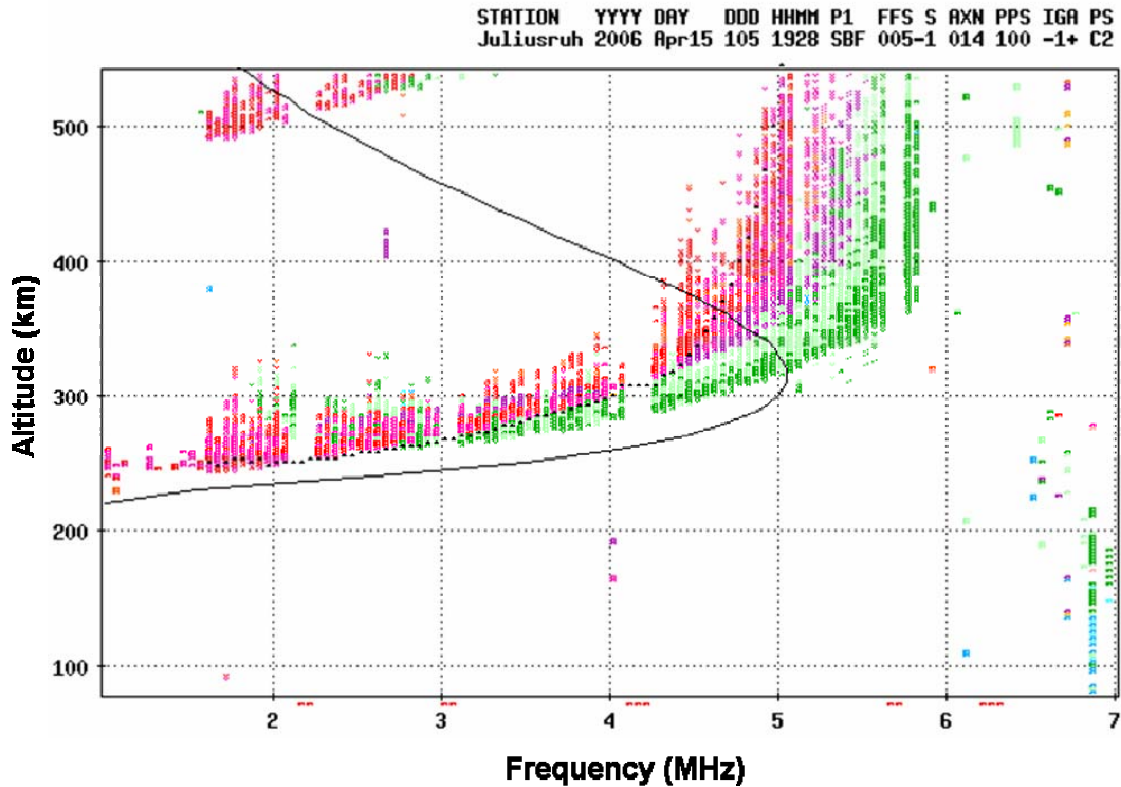
Figure 2: A real-time ionogram created from a vertical incident ionosonde in Juliusruh on 15 April 2006 by the Leibniz-Institute of Atmospheric Physics. The transmitter emits a sweep of frequencies, the receiver detects the refracted signals, and then a "virtual height of reflection" is calculated from the signals' travel time. The black line is the electron density profile computed from the virtual height. Colors denote strength of signal return (warm colors = stronger dB). The ionosphere above the F_2 peak cannot be measured from a vertical sounding, thus models are used to estimate this.

as a function of height at Wright-Patterson Air Force Base (WPAFB) throughout an entire day. The plasma frequency increases rapidly at sunrise (~ 1200 UT) due to photoionization and then decays after sunset (~ 2100 UT) when photoionization vanishes. In particular, notice how quickly the E layer decays after sunset. The rate of ionization is strongly dependent on solar zenith angle at altitudes where photochemical processes dominate, i.e. below the F_2 peak. The electron density above the F_2 peak is dependent not only on solar zenith angle, but also transport processes such as the magnitude of meridional neutral winds [*Schunk and Nagy*, 2000].

7
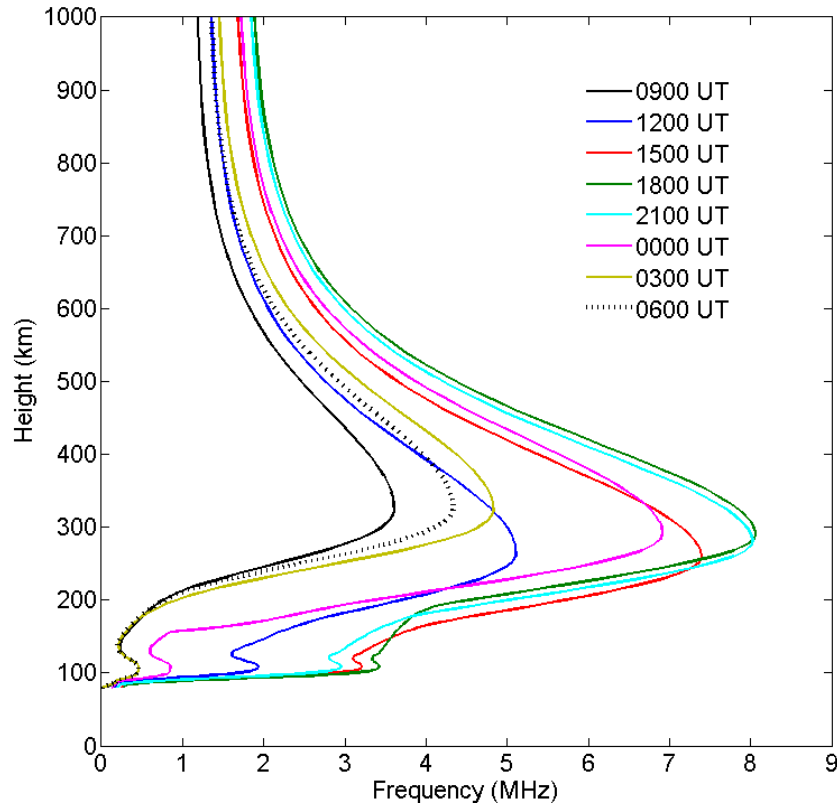
Figure 3: An example of the ionosphere's diurnal variation. Plasma frequency (MHz) as a function of height (km) at Wright-Patterson AFB on the autumnal equinox during normal solar and geomagnetic activity.

Considering that photoionization is the main source of ionization, it is logical that the ionosphere would display a strong seasonal variation as the solar zenith angle and hence photon flux changes throughout the year. Figure 4 gives an example of the seasonal variation in plasma frequency as a function of height at WPAFB at local noon. Notice that the plasma frequency is greater in winter than in summer, in spite of the fact that the solar zenith angle is greater in winter. This "seasonal anomaly" is due to the ionosphere's strong coupling with the neutral atmosphere, which also experiences seasonal fluctuations. An increased O/N_2 ratio in winter leads to a sufficient increase in the effective O^+ production rate, counteracting the solar zenith angle effect [*Schunk and Nagy*, 2000].

8
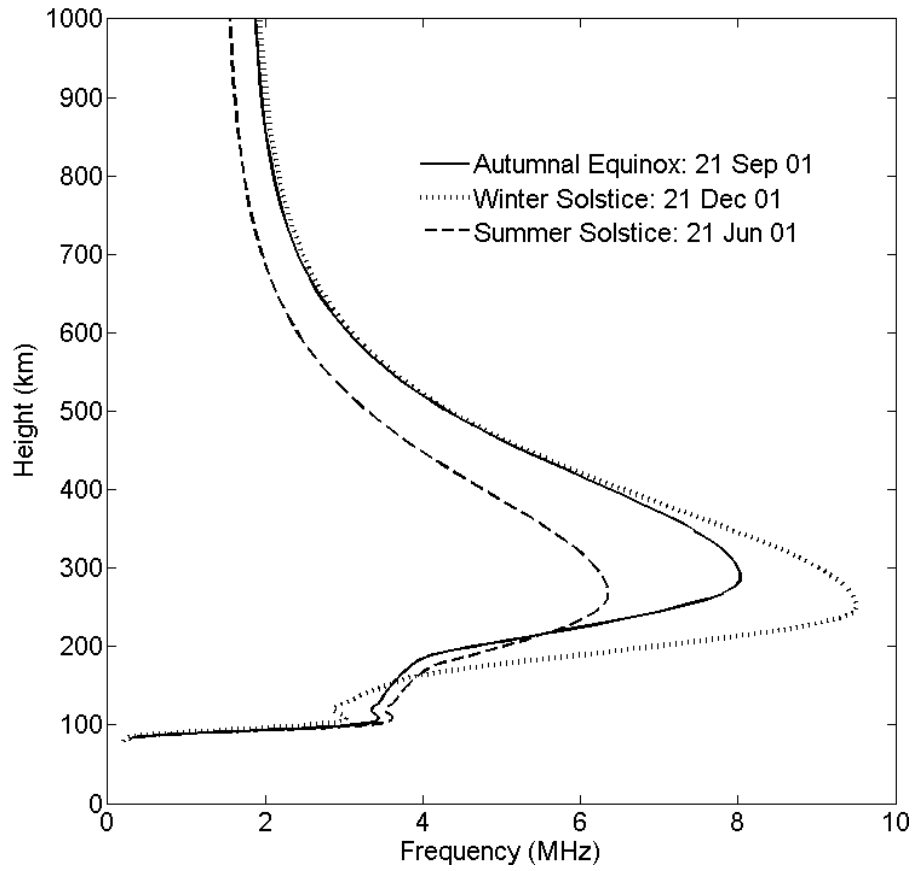
Figure 4: An example of the ionosphere's seasonal variation. Plasma frequency (MHz) as a function of height (km) for Wright-Patterson AFB at local noon on the autumnal equinox and solstices during normal solar and geomagnetic activity.

As with seasons, the solar radiation flux also varies with solar cycle. Solar EUV flux, which is the primary photon energy for photoionization, is significantly greater at solar maximum compared to solar minimum. Figure 5 shows an example of the solar cycle variation in plasma frequency as a function of height at WPAFB at local noon. The higher plasma frequencies (i.e. greater electron densities) at solar maximum are a result of changes in the neutral atmosphere as well as greater solar radiation flux amplifying the ionization rates.

9
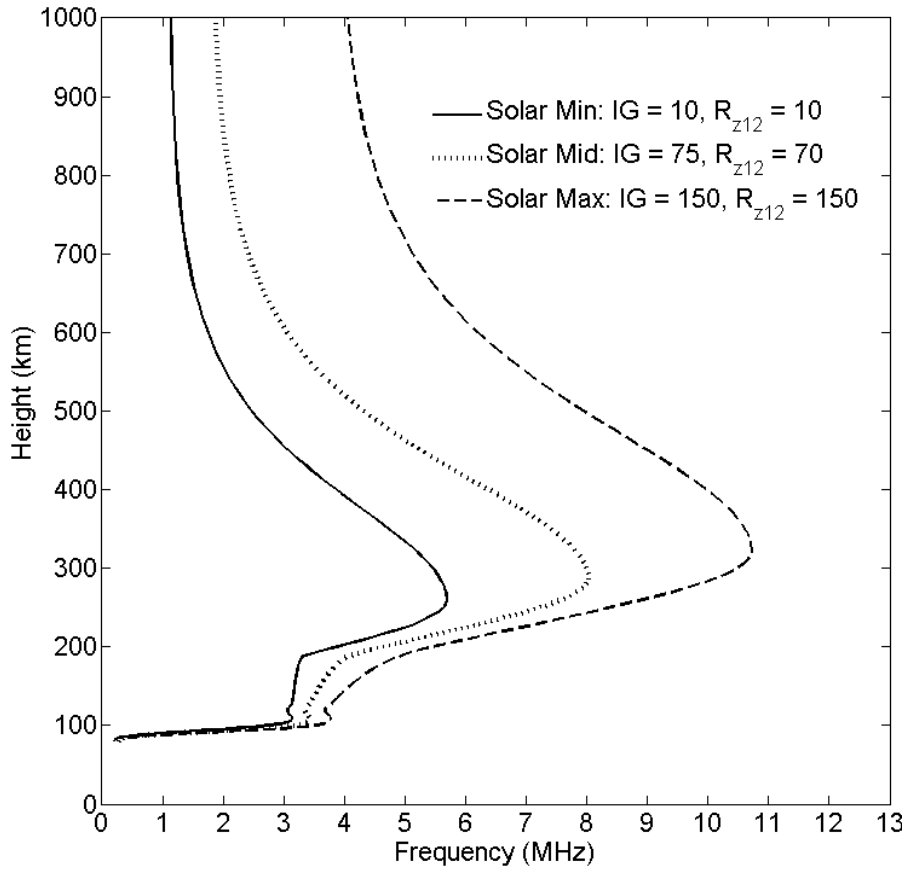
Figure 5: An example of the ionosphere's solar cycle variation. Plasma frequency (MHz) as a function of height (km) for Wright-Patterson AFB at local noon on the autumnal equinox during normal geomagnetic activity.

Irregular variations of the ionosphere include localized enhancements of the E region, known as a sporadic E layer. This layer can be flat and homogeneous or rather diffuse in size. An example of a sporadic E layer is seen in Figure 6. The electron density is plotted as a function of altitude and time, as measured by the Arecibo incoherent scatter radar [*Schunk and Nagy*, 2000]. There is a distinct sporadic E layer at 116 km, with a peak electron density of about 5×10^5 cm^{-3}. This layer persists after sunset (approximately 1800 local time) whereas the remainder of the region below the F_2 peak quickly decays. Since zonal neutral winds induce vertical ion drifts, any vertical wind shear will cause sporadic E layers to form where the drifts converge. Also seen in

10

Figure 6 is an "intermediate layer", which can appear in the lower F region at night (in this case 2030 local time) and gradually descends into the E region. In contrast to sporadic E layers, this layer is primarily formed by convergence of vertical ion drifts due to vertical wind shear of meridional rather than zonal neutral winds [*Schunk and Nagy*, 2000].
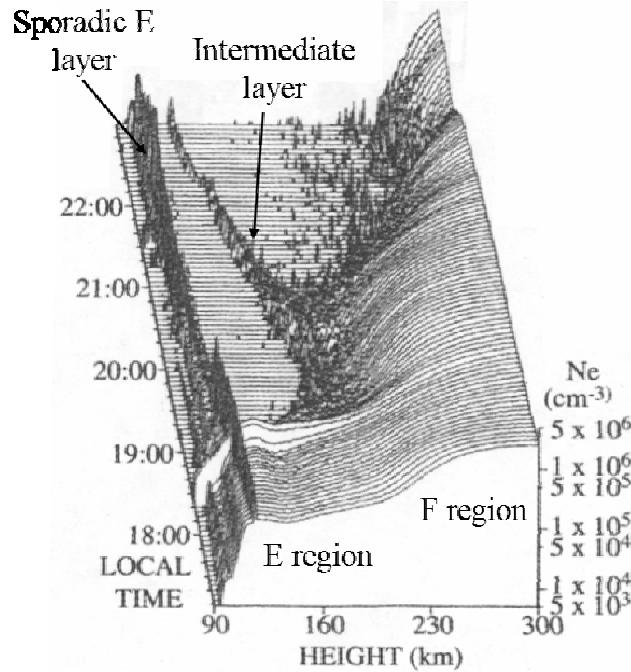
Figure 6: Ionospheric irregular variations. Electron density is shown as a function of both height and time. A sporadic E layer persists for the entire time period, while an intermediate layer begins to descend in height at approx 2000 LT. Density measured with Arecibo incoherent scatter radar on 7 May 1983. [*Schunk and Nagy*, 2000]

Another irregular variation of the ionosphere occurs during geomagnetic storms. In particular, the F region experiences a density enhancement during the initial (or positive) phase and then depletion during the main (or negative) phase of a geomagnetic storm. The cause of this effect is still not well understood. Although beyond the scope of this thesis, it is worth mentioning that the current hypothesis considers a combination of three mechanisms. First, variations in the neutral wind will raise or lower the

11

ionosphere, thereby changing the neutral atom/molecule ratios and thus the ion production/loss ratios. Second, the protonosphere's ability to act as a reservoir and "refill" the ionosphere at night is reduced during a geomagnetic storm. Third, heating from the magnetosphere via O^+ precipitation from the ring current increases the recombination rate [*Hargreaves*, 1992]. Figure 7 shows an example of the geomagnetic storm variation in plasma frequency as a function of height at WPAFB at local noon. The F region's plasma frequency decreases as the geomagnetic storm strength increases, characterized here by an increase in the 39-hr running average a_p index. The a_p index is
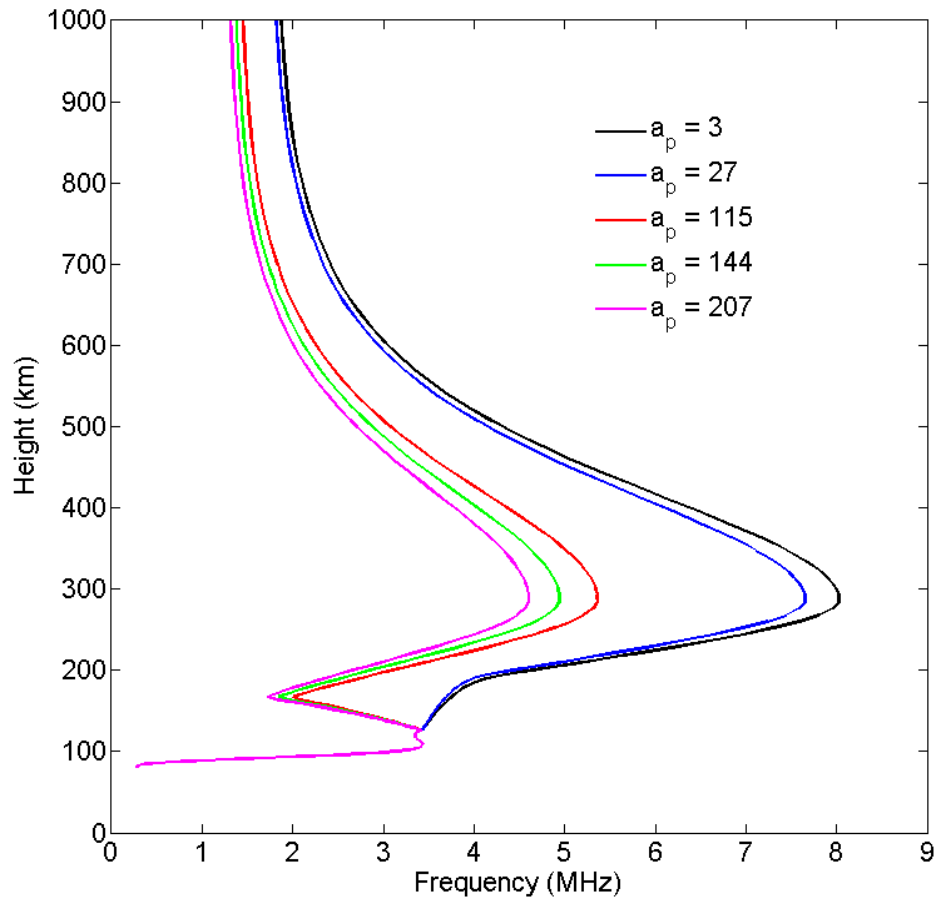
Figure 7: An example of the ionosphere's variation during the main (or negative) phase of a geomagnetic storm. Plasma frequency (MHz) as a function of height (km) for Wright-Patterson AFB at local noon on the autumnal equinox during normal solar activity. Note that the E layer peak at approx. 110 km is the result of an oversimplification in the IRI "storming" model and is not a realistic response of the lower ionosphere during storming conditions.

12

the linear equivalent to the K_p index, which is a quasi-logarithmic index of the 3-hourly range in magnetic field strength relative to a designated quiet-day curve, averaged and standardized for 13 mid-latitude geomagnetic observatories. Note that Figure 7 is created with the IRI-2001 model, which oversimplifies this effect by using a density scale factor above 165 km. The model is then forced to interpolate below 165 km, creating an unrealistic E layer at 110 km. A more detailed description of the IRI-2001 model will be given in a subsequent background section titled "Ionospheric Models".

Irregular variations in the ionosphere, such as sporadic E layers and F layer depletion during geomagnetic storms, can make accurate raytracing of HF signals considerably more difficult (if not impossible) due to their erratic behavior. The next section describes a few of the most important ionospheric effects on HF signal propagation.

Signal Propagation

Historic studies of HF signal propagation have revealed a wide range of interesting and now well-documented ionospheric effects, such as absorption, frequency shift, polarization shift, Faraday rotation, phase delay, group delay, and refraction. The latter effect has been identified as having the greatest influence on geo-location accuracy and therefore will be the focus of this section [*McNamara*, 1991]. We will see how refraction is directly proportional to electron density and how it affects signal propagation.

For simplicity, assume the signal is propagating within a cold, un-magnetized, plasma. Based on the development of *Sturrock* [1994], the refractive index, n , for this plasma is found to be the following:

13

$$n = \frac{c}{v_{phase}} = \sqrt{1 - \frac{\omega_{plasma}^2}{\omega_{signal}^2}} = \sqrt{1 - \frac{q^2 N_e}{\pi m_e \upsilon_{signal}^2}} \tag{2}$$

where c is the speed of light, v_{phase} the phase velocity, ω_{plasma} the angular plasma frequency, ω_{signal} the angular signal frequency, N_e the electron density, q the electron charge, m_e the electron mass, and υ_{signal} the signal frequency. Equation 2 indicates that the index of refraction approaches unity as the signal frequency approaches infinity or as the electron density goes to zero. This is the point at which no refraction occurs and the signal continues to propagate as it would in a vacuum. More importantly, the index of refraction approaches zero as the signal frequency approaches the plasma frequency, signifying the point at which the signal experiences maximum refraction.

Akin to geometric optics, the propagation of a signal between two media of differing refractive indices is given by Snell's Law,

$$n_i \sin \theta_i = n_r \sin \theta_r \tag{3}$$

The subscripts differentiate between the incident (i) and refracting (r) medium, while the angle θ is measured from the normal of the boundary. An illustration of this relation is seen in Figure 8.
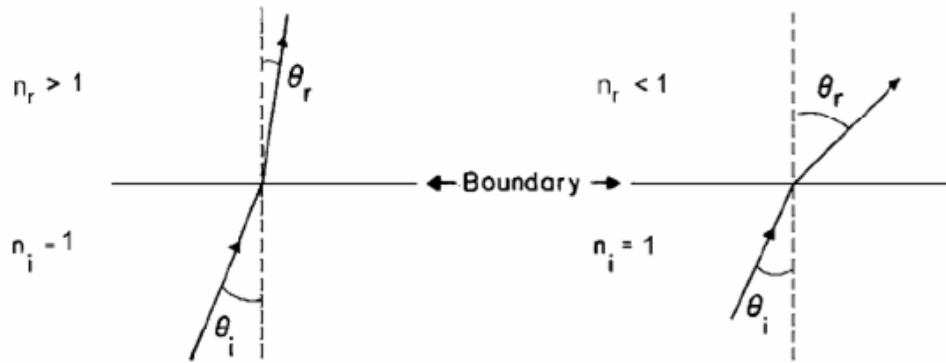
Figure 8: Snell's Law. Electromagnetic wave refracts away from the boundary normal when traveling into medium with smaller refractive index (seen on right side).

14

As a fixed-frequency signal propagates from a higher to lower electron density the refractive index of the plasma increases and the signal's phase velocity decreases, meaning the signal will refract toward the normal. Conversely, as the signal propagates from a lower to higher electron density the refractive index of the plasma decreases and the signal's phase velocity increases, meaning the signal will refract away from the normal. When conceptually applied to the ionosphere it is this latter case that ultimately leads to signal "reflection". If a signal is transmitted into an ideal ionosphere that can be characterized as a horizontally homogeneous slab consisting of stratified layers of increasing density (decreasing refractive index) with height, then Snell's Law says that the signal would eventually propagate perpendicular to the normal. It is at this point that Snell's Law breaks down, failing to explain how a signal is "reflected" by the ionosphere. Therefore, the signal needs to be treated as a wave in order for the signal to continue refraction back down to the original refractive index with the same angle of incidence, as seen in Figure 9. A more detailed description of this wave treatment will be given in a subsequent background section titled "Raytracing".
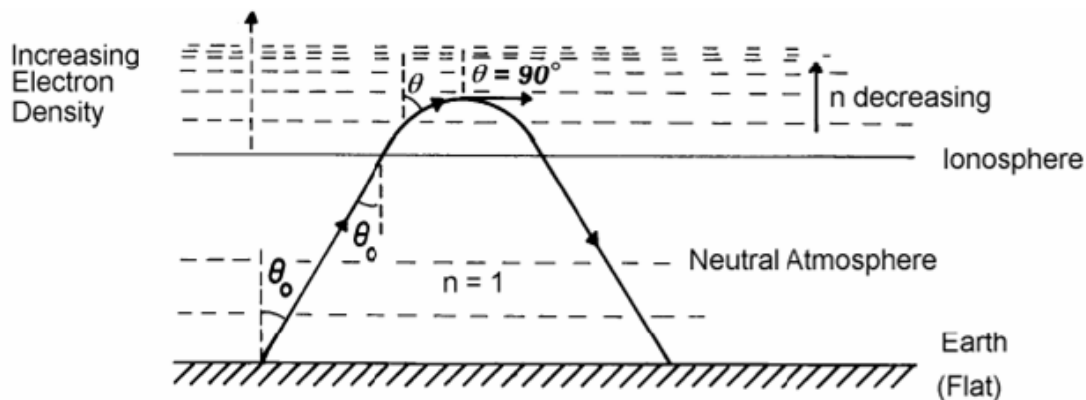
Figure 9: Application of Snell's Law in the ionosphere. The electromagnetic signal progressively refracts away from the boundary normal until the signal propagates perpendicular to the normal. Signal must be treated as a wave to account for continued refraction. Notice that the refractive index decreases with altitude, while the electron density increases with altitude.

15

Equations 2 and 3 indicate that higher signal frequencies require greater electron densities for refraction to occur. Since the refraction occurs later in the propagation, the signal path length increases. This relationship is seen in Figure 10, where the signal propagation paths are shown for increasing frequencies. Notice that higher frequencies eventually penetrate the ionosphere.
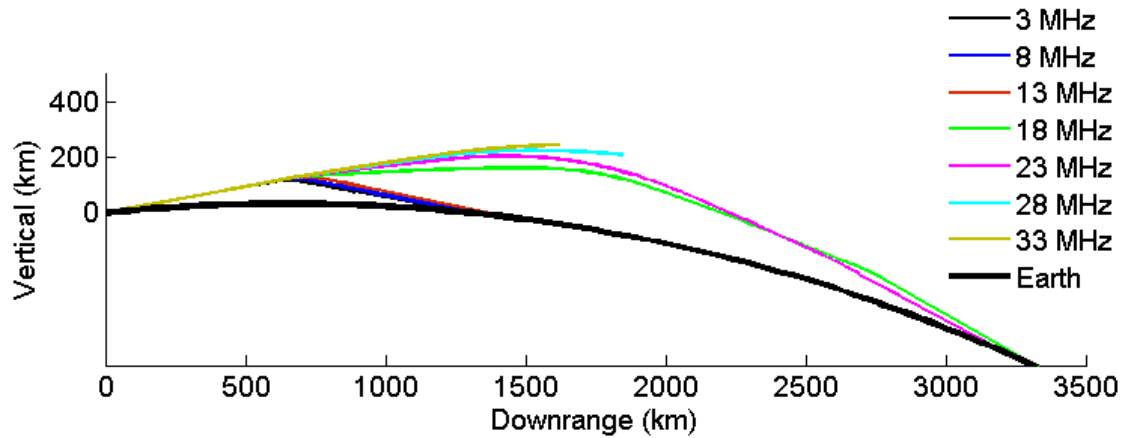
Figure 10: Dependency of signal propagation path on signal frequency. Greater electron densities are needed for higher frequencies to refract. The signal path length increases when refraction occurs later in the propagation. Higher frequencies eventually penetrate the ionosphere. Note that this assumes a horizontally homogeneous ionosphere.

Further examination of Equations 2 and 3 reveals a strong dependence on the elevation angle (measured from horizon; 90° - incident angle θ_i), and is illustrated in Figure 11. Initially the 12.45 MHz signal penetrates the ionosphere because its elevation angle is too large. Then the signal becomes progressively more refracted as the elevation angle decreases, eventually leading to "reflection". Notice that the altitude at which reflection occurs, hereafter called apogee height, begins to decrease as the elevation angle decreases. It is also interesting that the signal path length (and "first hop" ground range) initially decreases and then ultimately increases with smaller elevation angles. This behavior defines, in effect, a minimum ground range of approximately 1100 km for this

16

particular frequency and ionospheric state. In other words, the only way to propagate a signal to a location less than 1100 km away is to change the frequency, not the elevation angle.
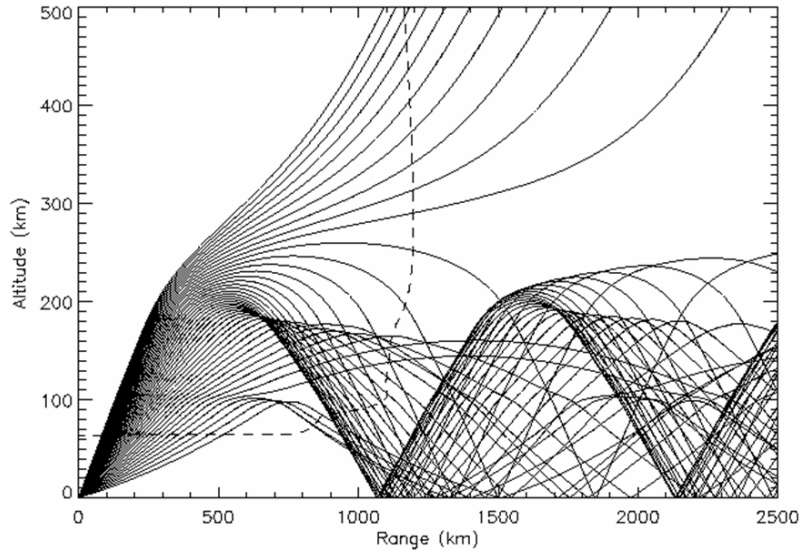
Figure 11: Dependency of signal propagation path on elevation angle. 12.45 MHz signal transmitted with elevation angles increasing from 5° – 50° (measured from horizon). Dashed line specifies the ionospheric density profile. Notice that the "reflection" altitude (apogee height) increases and the "first hop" ground range initially decreases then ultimately increases with larger elevation angles. [*Doherty*, 2004]

Adding a layer of complexity, assume that the signal now propagates within a magnetized plasma. The presence of the Earth's magnetic field introduces an effect known as magnetoionic splitting. Refer to *Budden* [1985] for the appropriate form of Equation 2 when a magnetic field is taken into account. Magnetoionic splitting differentiates the behavior of the ordinary and extraordinary propagation modes. Although this thesis focuses exclusively on the ordinary mode, it is still important to briefly describe the propagation behavior of the two modes. Figure 12 illustrates how a signal's ordinary mode deviates from its initial elevation angle (towards zenith) and eventually becomes perpendicular with the local magnetic field vector. This deviation towards the magnetic field also occurs when the signal is transmitted away from zenith.

17
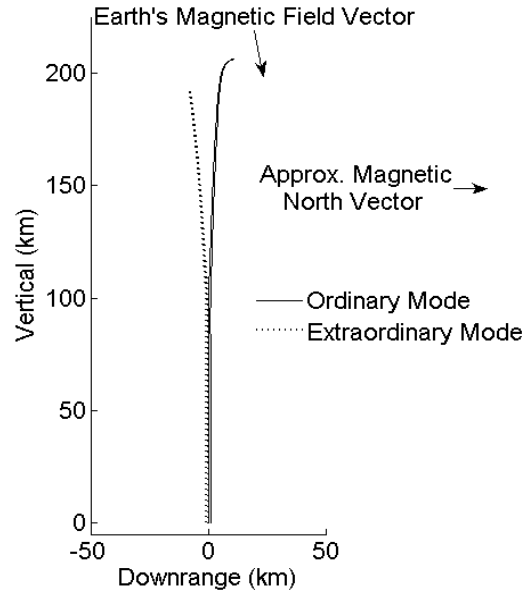
Figure 12: Magnetoionic splitting of a 5 Hz signal transmitted toward zenith from Wright-Patterson AFB at local noon on the autumnal equinox during normal solar and geomagnetic activity. The signal's propagation is affected by the local magnetic field. The signal's ordinary mode refracts to become perpendicular to the local magnetic field vector, while its extraordinary mode refracts to become parallel.

Figure 13 shows the crossrange track of a signal transmitted towards magnetic west as a function of distance downrange from the transmitter (i.e. propagation path projected onto x-y plane; note axes scale difference). The signal's ordinary mode begins to deviate towards magnetic north as it enters the ionosphere, reaches maximum crossrange at the point of "reflection", and then returns to the original transmission azimuth angle (measured from true north) as it exits the ionosphere. The same deviation occurs for transmission towards magnetic east. The magnitude of this deviation decreases as the transmission azimuth becomes more aligned with a magnetic meridian. In other words, there is no deviation when the signal is transmitted parallel to a magnetic meridian, such as from magnetic north to south or south to north. Both of these examples simply illustrate how propagation behavior is dependent on a signal's mode. Appendix A contains additional examples of magnetoionic splitting behavior.

18
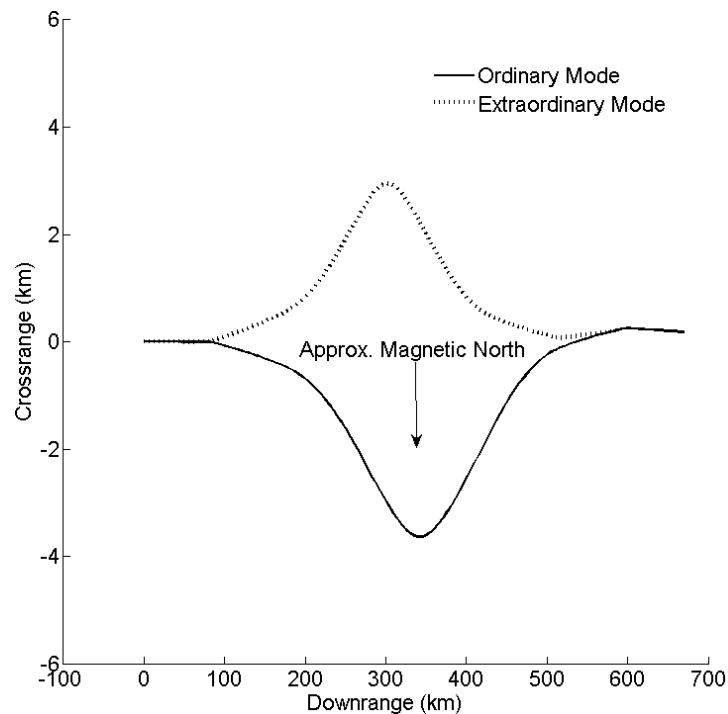
Figure 13: Magnetoionic splitting of a 10 MHz signal transmitted from Wright-Patterson AFB toward magnetic west at local noon on the autumnal equinox during normal solar and geomagnetic activity. Shown is crossrange (km) as a function of distance downrange (km). The signal's ordinary mode deviates toward magnetic north, while its extraordinary mode deviates toward magnetic south.

The strong dependence of HF signal propagation on the ionosphere's refractive index necessitates the capability to accurately model both the regular and irregular variations of the ionosphere. Therefore, it is important to understand the background of each ionospheric model used in this thesis and, in particular, how their designs differ.

Ionospheric Models

Three separate ionospheric models are used in this thesis. The first model is the 2001 update of the International Reference Ionosphere (IRI-2001) model. It is sponsored by both the Committee on Space Research (COSPAR) and the International Union of

19

Radio Science (URSI) and is often considered the standard for ionospheric parameters [*Bilitza*, 2001]. Being an empirical climatology model, it determines the dominant variations of ionospheric parameters from an existing observational database. Experimental observations from all available data sources, including ground and space, are used to predict a monthly average for each ionospheric parameter, assuming magnetically quiet conditions in a non-auroral ionosphere. Several solar indices are used as model input parameters. The 12-month running average of the sunspot number produced at the Zurich observatory (R_{z12}) is used for the F peak altitude and topside profile. Finally, the 39-hr running average of the a_p index is used to capture the F region depletion that occurs during a geomagnetic storm. IRI-2001 can also use real-time ionosonde data for better representation of the E region. It is worth noting that a newer version of IRI (after 2001) is being augmented to include TEC data inferred from GPS satellite data as another real-time input. Of the many IRI-2001 output parameters, this thesis only requires plasma frequency (i.e. electron density) as a function of position within a user-specified 3-D grid.

The second model is the Parameterized Ionospheric Model (PIM). Unlike IRI-2001, PIM is based on theoretical climatology rather than empirical climatology. While empirical models are, by their very nature, limited by the quantity and type of observed data, PIM produces a summary of the output of four physics-based numerical models parameterized for a variety of ionospheric conditions. *Daniell et al.* [1995] provides a concise description of the main difference between empirical and theoretical climatology:

> Empirical climatology yields an "average" ionosphere in which the average may be taken over very different ionospheric configurations. Persistent features such as the subauroral trough, auroral oval, or equatorial anomaly may be smeared out or broadened as a result of the averaging process …

20

> Theoretical climatology yields a "representative" ionosphere, i.e., an ionosphere that corresponds to a potentially realizable set of specific geophysical conditions. Ionospheric features will have locations, widths, amplitudes similar to those that might be observed on any given day under the specified geophysical conditions. Theoretical climatology is limited by the accuracy and completeness of the physics and chemistry included in the theoretical models on which it is based and the computer resources required to span the full range of geophysical conditions. [*Daniell et al.*, 1995]

Parameterization is accomplished in a two-step process. First, the four physics-based models created databases for distinct ionospheric conditions, such as various solar and geomagnetic activity levels. Then these databases were fit with semi-analytic functions to minimize storage space. PIM uses the R_{z12} index to estimate solar activity and the K_p index to estimate geomagnetic activity. For the purpose of this thesis, PIM's 3-D grid output of electron density is transformed into a 3-D grid of plasma frequency by using the relation found in Equation 1.

The third model is the new GPSII model introduced in Chapter I. Ionosondes can often be unavailable in a region of interest or their coverage may be too sparse to obtain an accurate specification of the ionosphere, especially in a combat environment. The GPSII model solves this problem by using passive measurements of the ionosphere. By analyzing data collected from dual-frequency GPS ground receivers, the GPSII model can estimate the TEC of the ionosphere along the many "lines of sight" between GPS satellites and ground receivers. (One TEC unit (TECU) = 10^{16} electrons per square meter integrated along the signal path.) Relative (or differential) TEC values are estimated by differencing the phase between the L1-band (1575.42 MHz) and L2-band (1227.6 MHz) GPS signals, while the absolute TEC data is estimated by differencing the group delay between the two signals. In order to correct for inherent error found in the data, the GPSII model accumulates statistics of both the GPS transmitter bias and receiver bias.

21

Either the IRI-2001 model or PIM can be used as its initialization (or background). Thus, its primary input parameters for solar and geomagnetic activity are the same as the input parameters of the particular model used for initialization; R_{z12}, IG_{12}, a_p, or K_p respectively. It then employs a Tikhonov inversion technique to convert the TEC data into a user-specified 3-D grid of plasma frequency. This inversion technique is an evolution of the technique developed for the Coordinate Registration Enhancement by Dynamic Optimization (CREDO) software package used in OTHR applications. *Fridman et al.* [2006] presents a more detailed discussion of the inversion technique and provides compelling evidence that the GPSII model's TEC-only specification can agree very well with actual ionosonde measurements. Although the GPSII model can incorporate ionosonde data into its inversion solution, this thesis focuses solely on its passive technique.

Geo-location

As mentioned in Chapter I, geo-location techniques can be divided into two main categories. The first technique uses several widely separated receivers to measure the signal's azimuth and triangulate the location of the transmitter. The second technique uses a single receiver to measure the signal's azimuth and elevation to determine the location of a transmitter, assuming that the ionospheric conditions along the signal's path are known. Refer to Figure 15 for an example. This latter technique is commonly referred to as single site location (SSL) and has several differing levels of complexity, ranging from a simple approximation to an extremely rigorous calculation.

The "classical" SSL method is considered the simplest approximation and can be used for medium-range applications (200 km – 500 km). This method assumes a signal is

22

reflected from a simple horizontal mirror at a particular height, based on fundamental laws of radio propagation in the ionosphere. The most important of these, conceptually, is Martyn's equivalent path theorem, which correlates a signal's oblique reflection with its vertical reflection. Referring to Figure 14, "the virtual height of reflection for vertical incidence is equal to the height of the equivalent triangular path for the oblique signal" [*McNamara*, 1991]. Ionograms made at the receiver can be used to infer the height of the "mirror" and thus the range to the transmitter (assuming the ionosphere is horizontally homogeneous), since ionosondes measure the virtual reflection heights as a function of signal frequency.
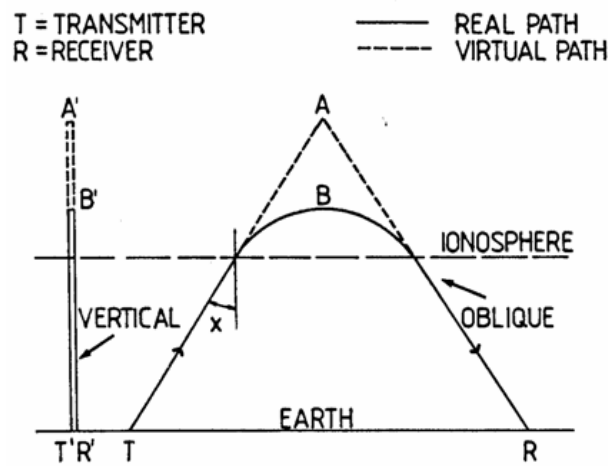
Figure 14: Martyn's equivalence path theorem. Correlates a signal's oblique reflection with its vertical reflection. [*McNamara*, 1991]

The classical SSL method has several weaknesses. Firstly, the ionogram made at the receiver is not a direct measure of the ionosphere where the signal refracts back downward. Secondly, we can only approximate the maximum height of the signal's path. Thirdly, Martyn's equivalence path theorem is exact only for a flat-Earth approximation [*McNamara*, 1991]. The equations used for the classical SSL method are further

23

complicated when the presence of the Earth's magnetic field is included. Refer to *McNamara* [1991] for an example application of the classical SSL method.

The "tilt correction" SSL method, which can be used for short-range applications (< 200 km), is considered slightly more complex. Horizontal gradients in electron density, conceptually visualized as a tilt in the ionosphere, can dramatically affect a signal's predicted ground range. There can be "synoptic tilts due to large-scale variations of the ionosphere with latitude and longitude, medium-scale tilts associated with traveling ionospheric disturbances (TIDs), and small-scale tilts with no obvious patterns" [*McNamara*, 1991]. The degree of tilt can be determined by an ionosonde measuring the angle of arrival of its own returning signals. A tilt correction is then applied to the classical SSL method, which now assumes that a signal is reflected from a simple tilted mirror at a particular height, as illustrated in Figure 15.
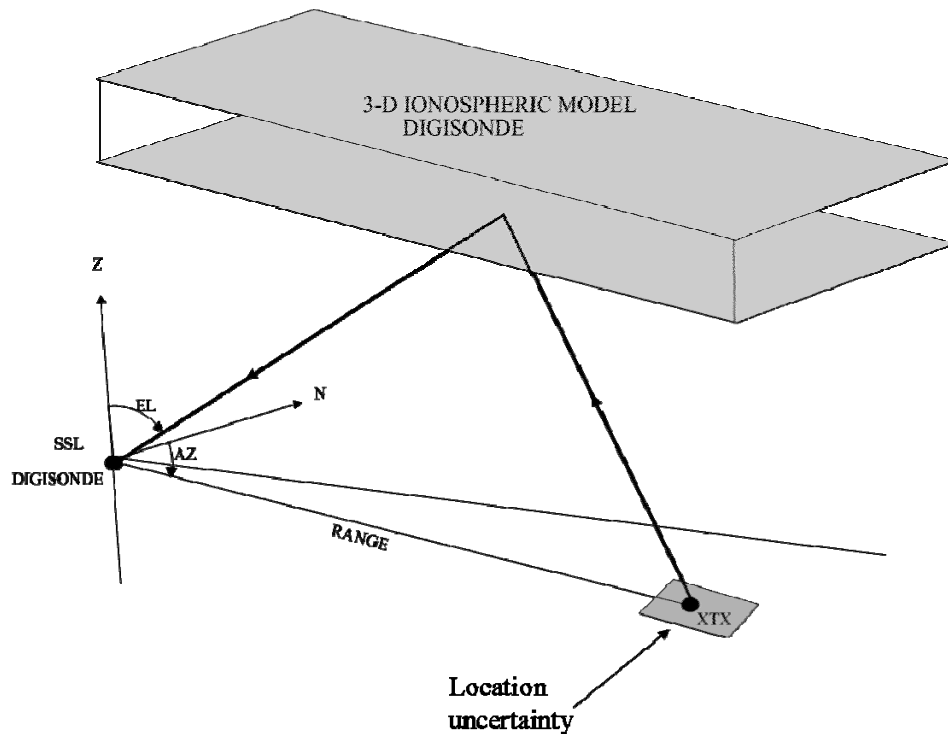
Figure 15: Short-range Single Site Location (SSL) technique using a three-dimensional tilted-slab ionosphere. (DRS Codem Systems, SSL presentation, 2006)

24

Raytracing, which can be used for long-range applications (> 500 km), is the most rigorous SSL method. As emphasized in the next section, raytracing relies heavily on having accurate knowledge of the ionosphere's electron density profile along the entire signal path. For that reason, a good ionospheric model becomes a crucial component. There can be many levels of raytracing complexity, depending on the ionospheric model's accuracy and the method of computation. Methods range from analytic raytracing with a simple one-dimensional non-magnetic ionosphere to numerical raytracing through a complex three-dimensional magnetic ionosphere. The theory and evolution of the numerical raytracing used in this thesis are presented in the next section.

Raytracing

The concepts found within geometrical optics eventually became the foundation for raytracing theory. In his third treatise supplement on geometrical optics, *Hamilton* [1832] introduced a set of differential equations that described the path of an electromagnetic signal through an anisotropic medium. In the dawn of the computer age, *Haselgrove* [1954] suggested that computers could numerically integrate Hamilton's equations and become "a new method for calculating ray paths in the ionosphere". Within a few years Haselgrove and her husband developed "a raytracing program to calculate 'twisted ray paths' through a model ionosphere using Cartesian coordinates" [*Haselgrove and Haselgrove*, 1960]. Further efforts came to fruition in 1975, when *Jones* and *Stephenson* [1975] developed a FORTRAN program to calculate a signal's three-dimensional path through an ionosphere whose refractive index constantly varied. We use an updated version of the Jones-Stephenson raytracing algorithm developed by Mark Hausman and L.J. Nickisch of NWRA.

25

Hamilton's differential equations have been derived using a variety of techniques throughout the years. Typically the form of the equations is dependent on their application, such as OTHR [*Coleman*, 1998] versus HF communications [*McDonnell*, 2000]. These equations are now collectively known as the "Haselgrove ray equation system" and are used within the Jones-Stephenson raytracing algorithm [*Huang and Reinisch*, 2006]. For the full derivation of these equations refer to *Jones and Stephenson* [1975] or *Nickisch* [1988]. This system of equations becomes considerably more complicated when the Earth's magnetic field is included. For a thorough description of propagation in the presence of a magnetic field refer to *Kelso* [1964], *Davies* [1989], or *Budden* [1985].

The equation set emphasizes how the signal's position and propagation vector are dependent on the ionosphere's index of refraction along the propagation path. The equations are numerically integrated at each step along the signal's propagation path, resulting in a new position and propagation vector for the signal at each successive step. The usefulness of this solution depends entirely on the accurate specification of the 3-D refractive index. Theoretically, we can measure the electron density as a function of position and then determine its refractive index by using Equation 2. However, it is impractical (and perhaps impossible) to fully specify the ionosphere through measurements alone, which is why ionospheric models are used to fill the gap.

Significant effort has been made by Hausman and Nickisch to ensure the raytracing algorithm works well with the models [*Fridman et al.*, 2006]. As a consequence of design, successful synthesis of the raytracing algorithm and the ionospheric models, especially when doing comparison studies, requires a disciplined

26

organizational structure. Furthermore, the visualization of the output depends upon software such as MATLAB®, as well as considerable programming experience. The next chapter describes the methods used to connect each of these components, as well as the reasons for particular case study selections.

Methodology

Overview

The primary objective of this thesis is to assess the impact of the three ionospheric models on HF signal raytracing during various ionospheric conditions. The secondary objective is to determine whether using passive techniques to model the ionosphere is sufficiently accurate for geo-location. Achieving these objectives require the integration of the ionospheric models, the Hausman – Nickisch update of the Jones – Stephenson raytracing algorithm, and MATLAB®. Figure 16 provides a summary of the flow of data between the components and the user.
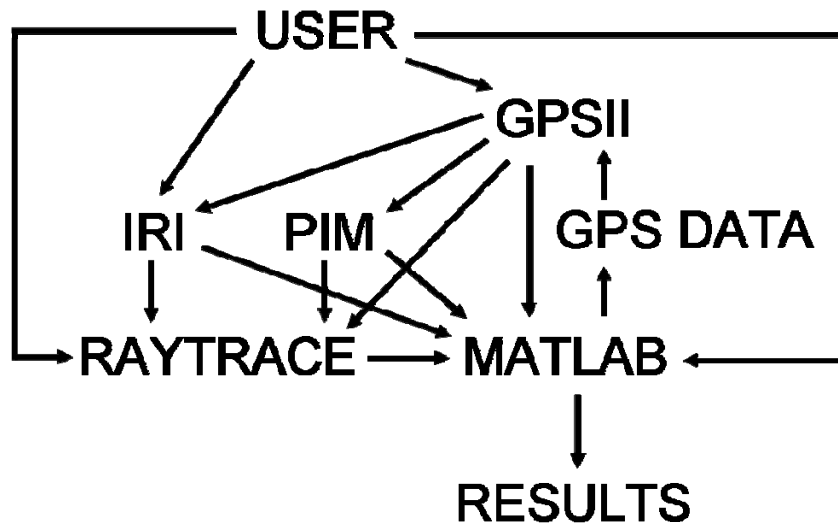
Figure 16: Summary of the flow of data between the user and the required components. The user directs the components to read initialization parameters, process data, and output results in proper formats for visualization and comparison.

This process is similar to that used by *Aune* [2006] in his study of trans-ionospheric raytracing. Each component requires interface with the user at various stages of the process. First, GPS data is collected for a user-defined region of interest using MATLAB®. Once initialized with user-defined parameters, the GPSII model produces

28

two ionospheric specifications. One is the background (initialization) model specification, while the other specification includes the TEC data. The raytracing algorithm's output includes the signal propagation path, which is processed and visualized using MATLAB®. The entire process is run on a Hewlett-Packard XW6200 Workstation configured with Windows XP, a 3.4 GHz Xeon processor, and 2 GB of RAM. The next sections provide a more detailed description of how each component is operated.

Ionospheric Models

A stand-alone IRI-2001 model is used to create idealized, horizontally homogeneous plasma frequency profiles for WPAFB. IRI-2001 model input parameters include the following: date and time of interest; region and resolution of interest; sunspot number and a_p indices, which are automatically determined by referencing a database file using the date and time of interest. Its output is a horizontally homogeneous plasma frequency profile for WPAFB. Many of the figures within Chapter II are produced using this model.

Similar to the stand-alone IRI-2001 model, the GPSII model is treated as a "black box". Yet, as expected with any model still under development, some anomalies in the GPSII model can arise throughout the research process. An official user's guide is now available from NWRA; it provides detailed information on the required file directory structure, input parameters, output files, and plotting options.

For this research, we focus on a 2000 x 2000 km region centered on WPAFB; this allows us to explore HF signal propagation distances of up to 1000 km from WPAFB. As recommended by NWRA, a latitude and longitude grid resolution of 0.5 degrees (~ 50

29

km) is used. In addition, a stepped altitude grid is selected for maximum resolution below the F_2 peak. Bearing in mind the time scales of most ionospheric behaviors, a time resolution of 15 minutes is adequate. The minimum distance between GPS ground receivers is set to a value (~ 250 km) that results in a maximum of 21 receivers to be used by the GPSII model. This upper limit on the number of used receivers is chosen in order to avoid system crashes due to computer processor/memory limitations, whilst ensuring sufficient TEC data availability. An example of GPSII input parameters are found in Appendix B.

The GPSII model is ran with a time interval of at least 12 hours so as to collect GPS satellite and ground receiver bias statistics for each particular day of interest. The model is then run again with a time interval of 24 hours (0000 UT – 2400 UT) using the previously collected bias statistics. Among its many output files are two ionospheric specifications, i.e. 3-D grids of plasma frequency. The first specification is that of the initialization model (either IRI-2001 or PIM), while the second includes the TEC data. These ionospheric specifications are then used by the raytracing algorithm to determine the propagation path of user-chosen HF signals.

Hausman – Nickisch Raytracing Algorithm

This update to the Jones-Stephenson raytracing algorithm is also treated as a "black box". Critical input parameters include the following: latitude/longitude of transmitter (WPAFB); signal frequency, azimuth angle, elevation angle, and signal mode; file name of 3-D plasma frequency grid. An example of these input parameters, as well as many others, is shown in Appendix C. For additional guidance on the algorithm's operation, refer to the unofficial user's guide written by *Aune* [2006] or to the official

30

user's guide provided by NWRA. The raytracing code produces the 3-D position of the HF signal along its entire propagation path, from the transmitter to where it impacts the Earth's surface (receiver). Note that the raytracing code can also calculate multiple hops of a signal. This data is then ingested and visualized using MATLAB®.

Case Study Selection

Five case studies are used to assess the impact of various ionospheric models on HF signal raytracing. These case studies cover an assortment of ionospheric conditions, ranging from quiet conditions to solar flares and geomagnetic storms. Specific signal frequencies are chosen in order to avoid ionospheric penetration, which is dependent on the particular case study's ionospheric conditions. This also holds true for a signal's elevation angle of transmission. As a reminder, this thesis examines only a signal's ordinary mode of propagation and not its extraordinary mode.

Case study #1 is chosen in an effort to isolate the effect that the E layer has on signal propagation and geo-location. As described in the previous section, the stand-alone IRI-2001 model is used to create an idealized, horizontally homogeneous ionosphere. This ionosphere is then manually adjusted to have either a significant E layer or no E layer at all. For our "base reference", we design case study #2 to compare the ionospheric models at local noon on a day with totally quiet solar and geomagnetic conditions.

As for the remaining three case studies, our approach is to isolate certain ionospheric drivers. For example, case study #3 focuses simply on the daily variability of the ionosphere at local noon during seven consecutive days of very low solar and geomagnetic activity. Meanwhile, case study #4 investigates a strong X3 solar flare that

31

occurred on 15 July 2002 during low geomagnetic activity. This particular event is chosen so that we can completely isolate the ionosphere's response to only that of the flare. Finally, case study #5 explores an intense geomagnetic storm that occurred on 27 August 1998. This event is chosen because there are no significant solar flares throughout its duration. The unique qualities of this geomagnetic storm allow us to completely isolate the ionosphere's response to only that of the geomagnetic storm. Tables 1, 2, and 3 contain specific information regarding each case study, such as their time(s) and date(s) of interest, corresponding ionospheric indices, and signal raytracing parameters.

Table 1: Dates and times of interest for each case study.

Case	Name	Time (UT)	Date
1	E layer Effect	1730	21-Sep-01
2	Quiet Condition	1745	9-Jan-06
3	Daily Variability	1745	8-Jan-06 - 14-Jan-06
4	Solar Flare	2000, 2015, 2215	15-Jul-02
5	Geomagnetic Storm	0045, 0245	27-Aug-98

Table 2: Ionospheric models and indices for each case study, including IG, R_{z12}, running 39-hr average a_p, K_p, and number of each solar flare type.

Case	Ionospheric Model Used	IG / Rz12	Running 39-hr avg ap / Kp	Flare (C / M / X)
1	IRI, GPSII	75.0 / 70.0	115.0 / 6.66	6 / 0 / 0
2	IRI, GPSII	20.6 / 20.8	2.5 / 0.00	0 / 0 / 0
	PIM, GPSII	20.6 / 20.8	2.5 / 0.00	0 / 0 / 0
	Unphysical IRI, GPSII	150.0 / 150.0	115 / 6.66	0 / 0 / 0
3	IRI, GPSII	20.6 / 20.8	0.9 - 4.8 / 0.00 - 1.66	all 0 / 0 / 0
4	IRI, GPSII	135.0 / 102.7	3.4 / 1.66	8 / 1 / 1
	PIM, GPSII	135.0 / 102.7	3.4 / 1.66	8 / 1 / 1
5	IRI, GPSII	70.4 / 67.8	110.1 / 7.00	2 / 0 / 0
	PIM, GPSII	70.4 / 67.8	110.1 / 7.00	2 / 0 / 0

Table 3: Signal parameters used in raytracing for each case study, including frequency, elevation (measured from horizon), azimuth (measured from true north), and mode.

Case	Freq (MHz)	Elevation (deg)	Azimuth (deg)	Mode
1	6, 8	35.000	180.000	O
2	7	31.166	115.755	O
3	7	31.166	115.755	O
4	8	40.260	116.418	O
5	5	38.657	116.042	O

32

Results

Case Study #1: E layer Effect

The first case study examines how the E layer affects HF signal propagation. As described in the previous chapter, we create two horizontally homogeneous ionospheres; identical above the E region, but differing significantly within the E region. One has a strong E layer, while the other has no E layer. Refer to Table 2 for the various ionospheric indices that are used to generate these. The plasma frequency profiles for both cases are shown in Figure 17; the figure represents the ionosphere over WPAFB at local noon.
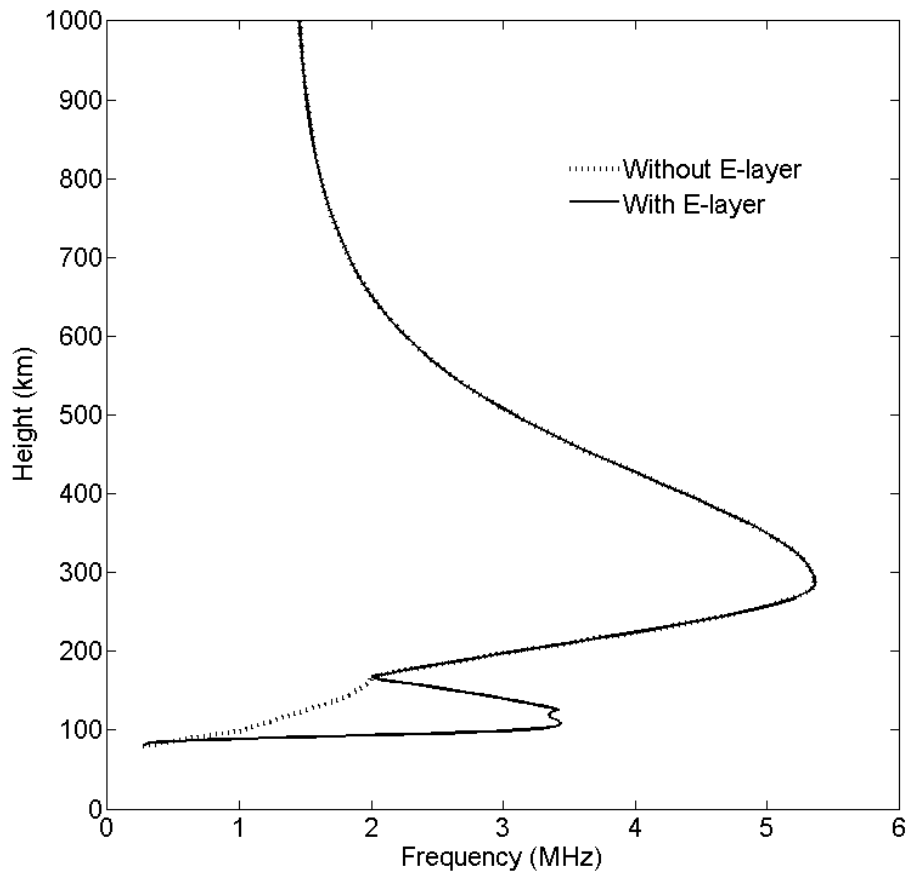

Figure 17: E layer variation. Plasma frequency (MHz) as a function of height (km) for Wright-Patterson AFB at local noon on the autumnal equinox during fictitious solar and geomagnetic conditions.

33

We simulate the transmission of both a 6 MHz and 8 MHz signal through these idealized ionospheres. Refer to Table 3 for the specific signal parameters that are used for the raytracing. The resulting propagation paths, projected onto the x-z plane, are seen in Figure 18 (top = 6 MHz, bottom = 8 MHz). The signals have a simple, quasi-parabolic trajectory when the E layer is negligible. Their trajectories become more complex when a non-negligible E layer is added. The signals begin to refract earlier in their propagation as they encounter the higher plasma frequencies of the E layer. They continue propagating through the E layer and eventually refract back toward Earth due to the F layer. Notice that the maximum height of their propagation path is exactly the same, irrespective of E layer magnitude. This is because the two ionospheres have the same plasma frequencies above 165 km, where the majority of the refraction occurs. The signals are refracted again by the E layer as they return to the Earth's surface. The resulting "wavy" trajectories seen in Figure 18 are thus due to the presence of the E layer. More importantly, the signals' ground ranges increase by this effect because the refractions occur earlier in their propagation. The ground range of the 6 MHz signal increases by 165 km, while the ground range of the 8 MHz signal increases by 47 km. The increase is less for the 8 MHz signal because its frequency is higher relative to the plasma frequency of the E layer.

The upper and lower limits of this "E layer effect" can be found by increasing or decreasing the signal frequency. Lowering the frequency increases the ground range until the frequency becomes low enough to be "reflected" by the E layer. Raising the frequency decreases the ground range offset until it eventually matches the negligible E layer case (assuming that the higher frequency does not penetrate the F layer).

34
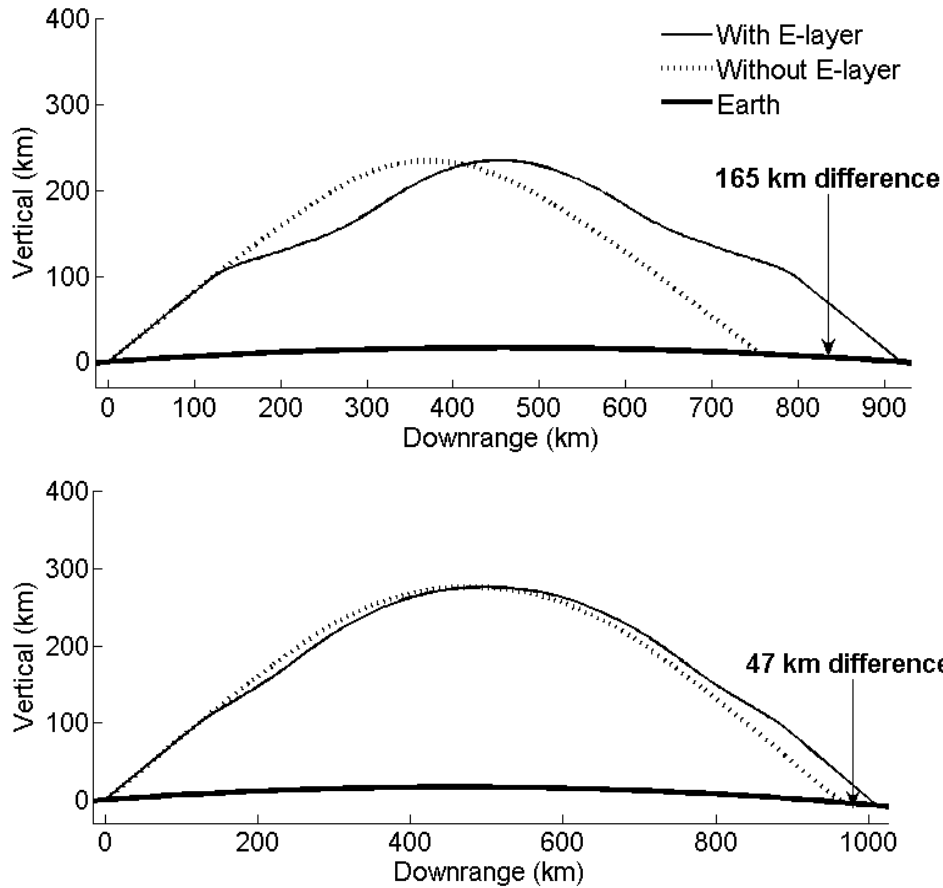
Figure 18: Effect of E layer on signal propagation for two different frequencies. Signals are transmitted with elevation = 35° and azimuth = 180° from Wright-Patterson AFB, OH at local noon on the autumnal equinox during fictitious solar and geomagnetic conditions. Their propagation paths are shown projected onto the x-z plane. Top trajectory is for a 6 MHz signal; bottom trajectory is for an 8 MHz signal. Presence of E layer increases the signals' propagation path (signals return to Earth further downrange). This effect is dramatically less for the slightly higher signal frequency.

This case study underscores the significance of the E layer to the ground range and its potential impact on the geo-location mission. Therefore, it is critical that we obtain the most accurate specification of the lower ionosphere, particularly for lower frequencies. In the remaining case studies we will focus on how well each of the three ionospheric models specifies the lower ionosphere under various ionospheric conditions.

Case Study #2: Quiet Conditions

The second case study establishes a "base reference" by comparing the three ionospheric models, and corresponding raytrace results, for quiet solar and geomagnetic conditions. Local noon on 9 Jan 06 is selected to represent our quiet conditions. Refer to Table 2 for the various ionospheric indices that describe this day. Figure 19 shows the critical frequency contours (MHz) for local noon on 9 Jan 06 using the various models. The left column depicts the results of the initialization model (IRI-2001 or PIM). The right column is the GPSII model, using the corresponding initialization from the left column. The middle row represents IRI-2001 and GPSII model results when unphysical initialization conditions are used (compared to the actual quiet conditions of 9 Jan 06). The intention is to gauge how well the GPSII model uses the measured TEC data to adjust for unphysical initialization. The triangles indicate the position of GPS ground receivers used in the GPSII model specification, while the crosses show the position of ionospheric pierce points (at 400 km) for each satellite-receiver path.

There is a distinctive, consistent pattern throughout all of the GPSII model critical frequency contours. The inner regions of plots have the most ionospheric pierce points, with the outer few degrees (latitude/longitude) of the plots lacking them entirely. Therefore, the most TEC data-driven model adjustments occur in the center of the grid. Consequently, the GPSII model reverts to the initialization model along the outer boundary. This produces a subtle "bulls-eye" pattern, which was originally recognized and described by *Fridman et al.* [2006].

The critical frequency contours of the IRI-2001 model (top left) and PIM (bottom left) initialization are remarkably similar. The GPSII model with IRI initialization (top

36
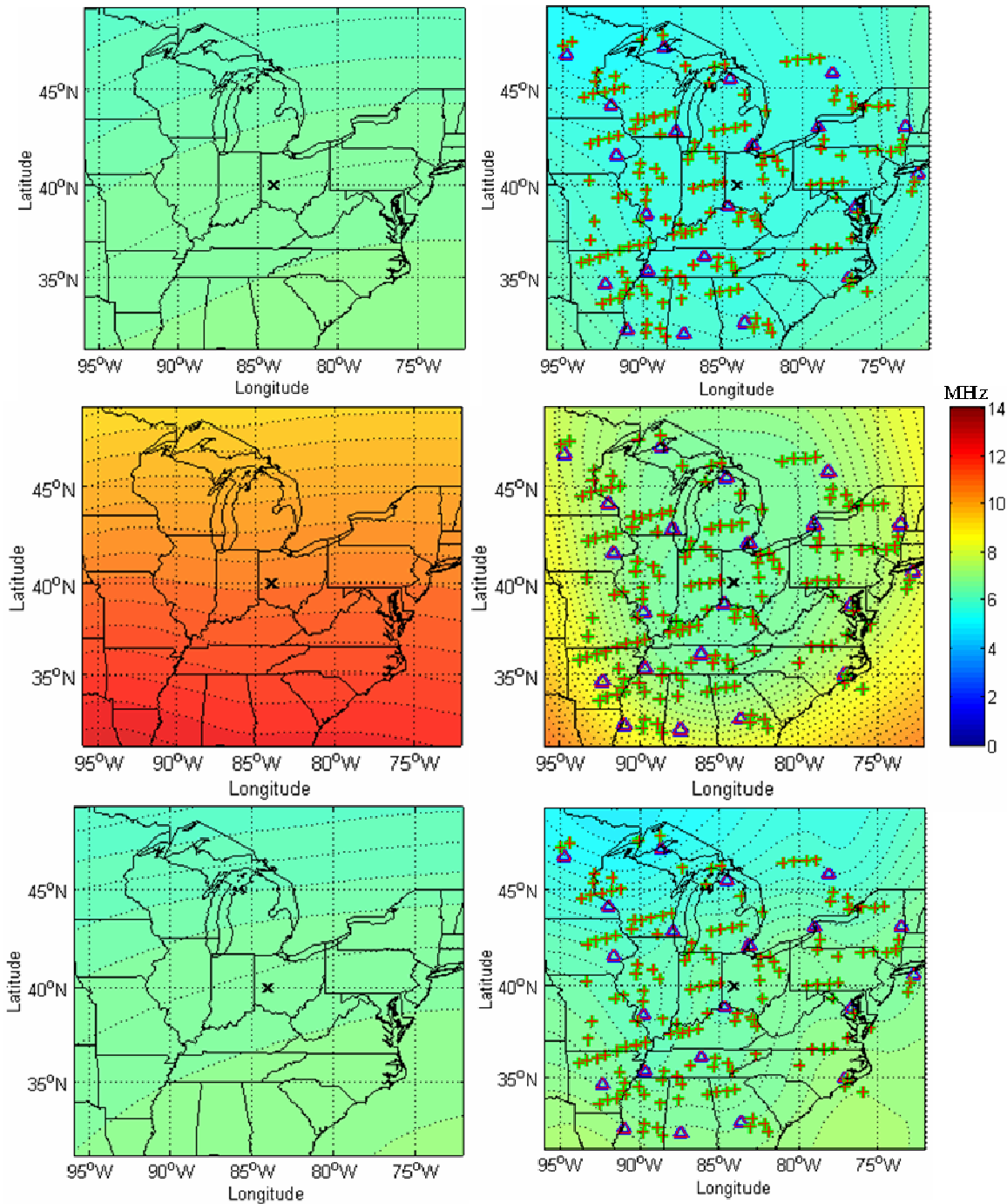
Figure 19: Critical frequency contours (MHz) at local noon on 9 Jan 06 (quiet solar and geomagnetic conditions). Left column is the initialization model. Right column is the GPSII model using the initialization model from the left column. Top row uses IRI-2001 initialization. Middle row uses unphysical initialization conditions compared to the actual quiet conditions of 9 Jan 06, showing how the GPSII model adjusts for unphysical initialization. Bottom row uses PIM initialization. Triangles indicate position of GPS ground receivers and crosses show position of ionospheric pierce points (at 400 km) for each satellite-receiver path.

37

right) has overall lower critical frequencies compared to the IRI-2001 model (top left) by approximately 2 MHz. Meanwhile, the GPSII model with PIM initialization (bottom right) only has these lower critical frequencies in the upper region of the plot compared to PIM (bottom left). The two GPSII model specifications (top and bottom right) have roughly the same contour pattern, disregarding the "boundary effect" described earlier.

A signal is transmitted from WPAFB toward Norfolk, VA in anticipation of future ground truth data validation. Refer to Table 3 for the specific signal parameters that are used for the raytracing. Figure 20 shows the plasma frequency profiles at the signal's approximate apogee for each of the six runs described in Figure 19.

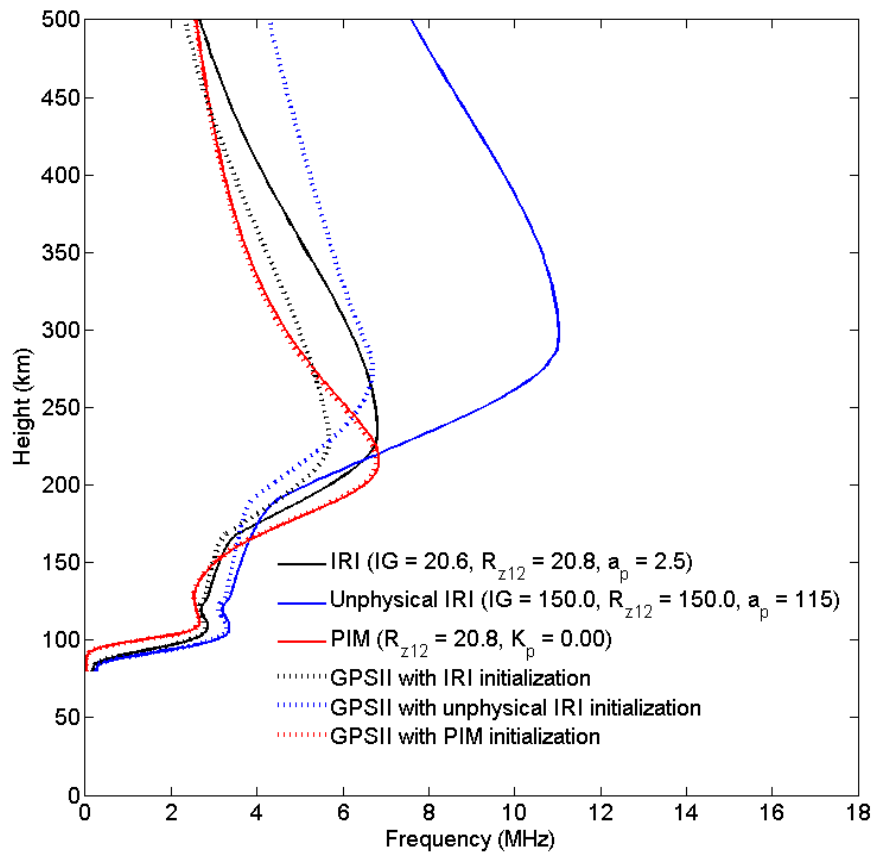**Figure 20: Plasma frequency (MHz) as a function of height (km) at the approximate apogee of a signal transmitted from Wright-Patterson AFB, OH toward Norfolk, VA at local noon on 9 Jan 06 (quiet solar and geomagnetic conditions) using various ionospheric models. The IRI model representing unphysically active conditions compared to actual quiet conditions is shown in blue.**

38

Examining Figure 20, it is interesting to note in regards to the topside ionosphere (above the F_2 peak) that the GPSII model makes significant adjustments to the IRI-2001 model initialization, especially when the unphysical conditions are used (comparing black/blue solid lines to dotted lines). In contrast, very little adjustment is made when the GPSII model uses PIM for its initialization. In the lower ionosphere (below the F_2 peak), the GPSII model once again makes the least adjustment when it is initialized with PIM, increasing the plasma frequency by no more than 0.25 MHz. All of the models have relatively the same E region profiles. The unphysical IRI-2001 model has a slightly more pronounced E layer in response to the higher indices that are used as its inputs.

Perhaps most interesting, the GPSII model does not make any significant adjustments to the E layer, regardless of the initialization. This suggests that using TEC data does not assist in specifying the E layer. A logical explanation of why TEC data does not provide any E region information requires a closer look at the definition of TEC. Vertical TEC (rather than slant TEC along the satellite/receiver path) is simply the integration of the electron density with respect to altitude. Instead of the usual plasma frequency profile, imagine a plasma density profile in linear coordinates. Remember from Equation 1 that the plasma density is proportional to the square of its frequency. The vertical TEC can then be represented as the integrated area to the left of the density profile. Analyzed in this way, the contribution of the E region to vertical TEC is considerably small and almost negligible. Therefore, it is extremely difficult, if not impossible, to extract E region information from TEC measurements alone. Keeping this in mind, it is doubtful that the GPSII model's passive technique by itself can provide any better specification of the E layer.

39

Figure 21 shows the resulting propagation path of an HF signal projected onto the x-z plane for all model runs except the unphysical IRI-2001 model. Refer to Table 3 for the specific signal parameters that are used for the raytracing. We find little difference between the trajectory that is computed using PIM and the trajectory computed using the GPSII model with PIM initialization (red lines). This is because there is very little difference between the two ionospheric profiles, as mentioned earlier. There is a bigger difference between the other two trajectories due to a larger divergence in their respective ionospheric profiles below 175 km.
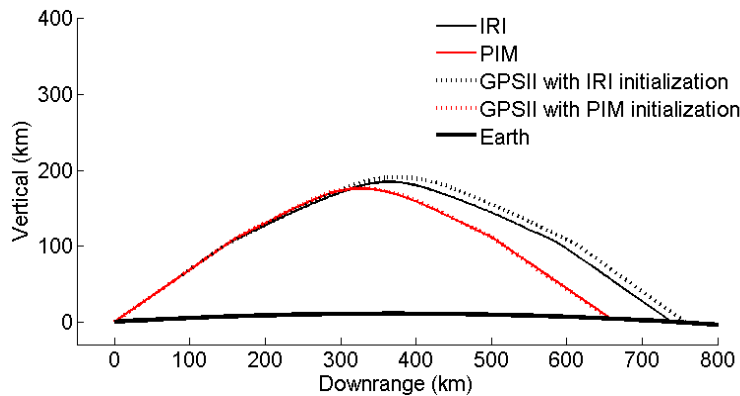
Figure 21: Propagation path projected onto the x-z plane for a 7 MHz signal transmitted from Wright-Patterson AFB, OH toward Norfolk, VA at local noon on 9 Jan 06 (quiet solar and geomagnetic conditions) using various ionospheric models.

The corresponding receiver locations are shown in Figure 22. A receiver location is defined as the point where the signal impacts the Earth's surface. The GPSII model adjusts the receiver location by approximately 20 km from that of the IRI-2001 initialization and only 3 km from that of PIM initialization. Since the GPSII model uses TEC data to create a more realistic specification of the ionosphere, we would expect to see the receiver locations "converge" toward a common location, regardless of its initialization. Instead, the receiver locations seen in Figure 22 actually "diverge" when the GPSII model is used.

40
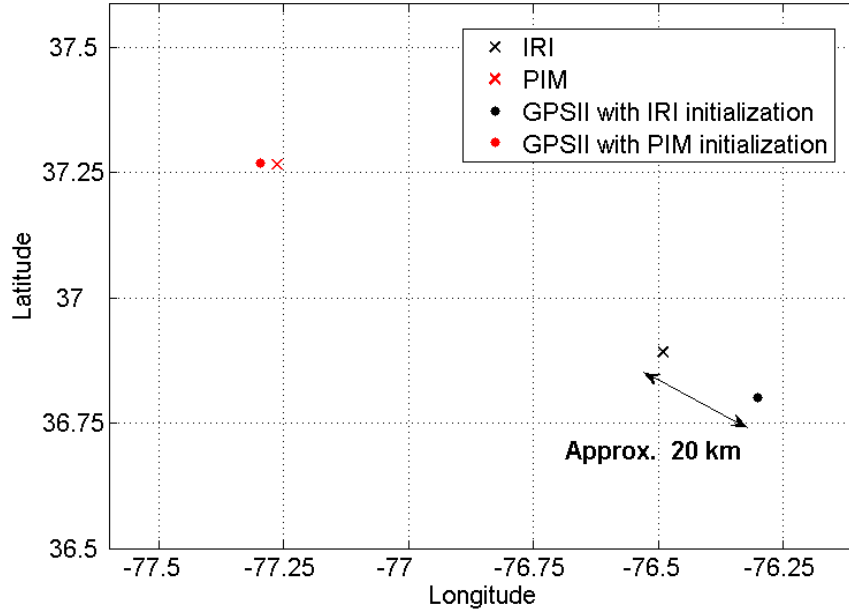
Figure 22: Receiver location (where a signal returns to the Earth's surface) for a 7 MHz signal transmitted from Wright-Patterson AFB, OH toward Norfolk, VA at local noon on 9 Jan 06 (quiet solar and geomagnetic conditions) using various ionospheric models.

This case study shows that the GPSII model is able to adjust for an unphysical initialization, yet more importantly that the GPSII model may not be able to aid in specifying the E layer. As far as quiet conditions are concerned, the GPSII model makes the smallest adjustments when initialized with PIM.

Case Study #3: Daily Variability

With an established reference for quiet conditions, we next examine how the models represent the daily variability of the ionosphere and how this variability affects geo-location. We examine local noon over seven consecutive days of very low solar and geomagnetic activity. Refer to Table 2 for the various ionospheric indices that describe the conditions during this week of interest.

Figure 23 shows the plasma frequency profiles at the approximate point of apogee of a signal transmitted from WPAFB toward Norfolk, VA for local noon during the week

41

of interest using the IRI-2001 and GPSII models. The profiles of the IRI-2001 model are tightly grouped and steadily decrease in plasma frequency throughout the week due to changes in both the solar zenith angle and neutral atmosphere. In contrast, the profiles of the GPSII model are erratic and have no trend in plasma frequency fluctuations, especially in the lower ionosphere where maximum refraction of HF signals occurs (see inset of Figure 23).
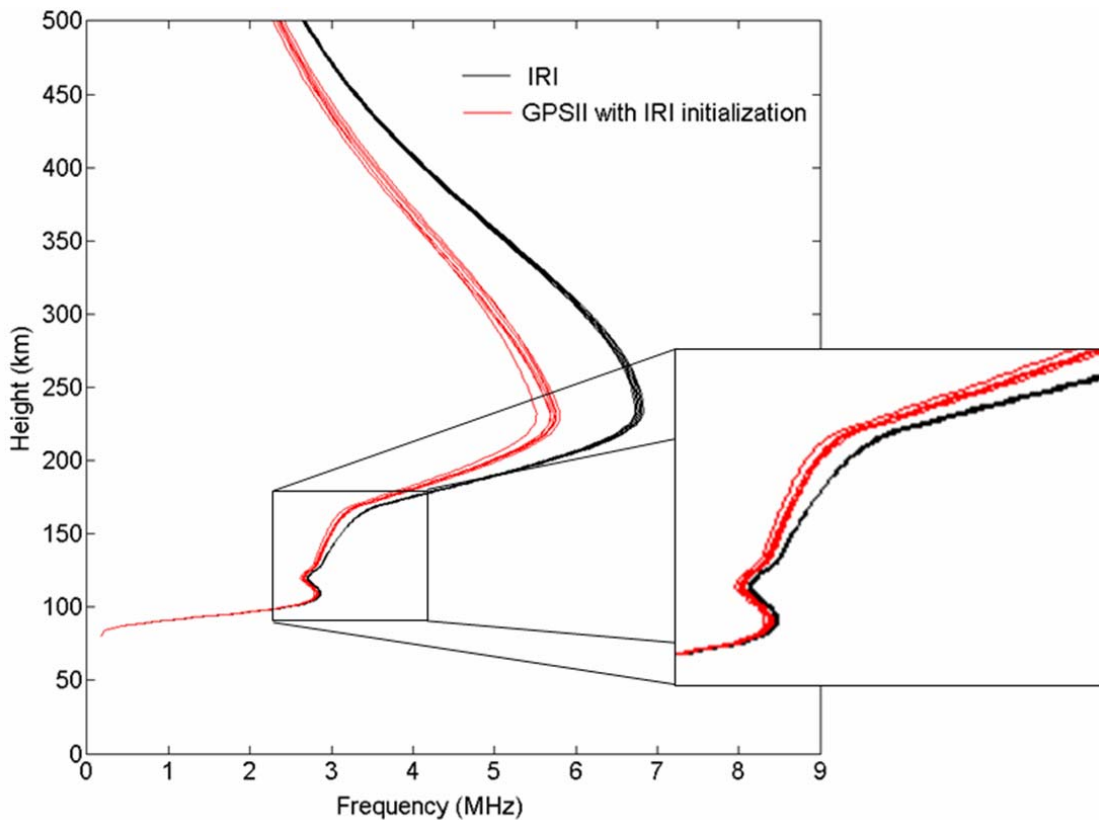
Figure 23: Plasma frequency (MHz) as a function of height (km) at the approximate apogee of a signal transmitted from Wright-Patterson AFB, OH toward Norfolk, VA at local noon during the week of 8 – 14 Jan 06 (very low solar and geomagnetic activity) using the IRI and GPSII models.

Figure 24 shows the crossrange as a function of distance downrange (from the transmitter) of an HF signal transmitted from WPAFB toward Norfolk, VA at local noon during the week of interest. Refer to Table 3 for the specific signal parameters that are used for the raytracing. The crossranges of the IRI-2001 model are once again tightly grouped, varying by less than 0.1 km at the end of the signal path. Meanwhile, the crossranges of the GPSII model vary markedly throughout the week, differing by over 1 km at the end of the signal path.

Figure 24: Crossrange (km) as a function of distance downrange from the transmitter (km) of a 7 MHz signal transmitted from Wright-Patterson AFB, OH toward Norfolk, VA at local noon during the week of 8 – 14 Jan 06 (very low solar and geomagnetic activity) using the IRI and GPSII models.

The corresponding receiver locations are shown in Figure 25. The receiver locations of the IRI-2001 model are shifted by a consistent 1 km step to the southeast each day. This is due to the steady decrease in plasma frequency of the IRI-2001 model throughout the week as the solar zenith angle decreases. In stark contrast, the receiver locations of the GPSII model are highly variable, differing by as much as 5 km per day.
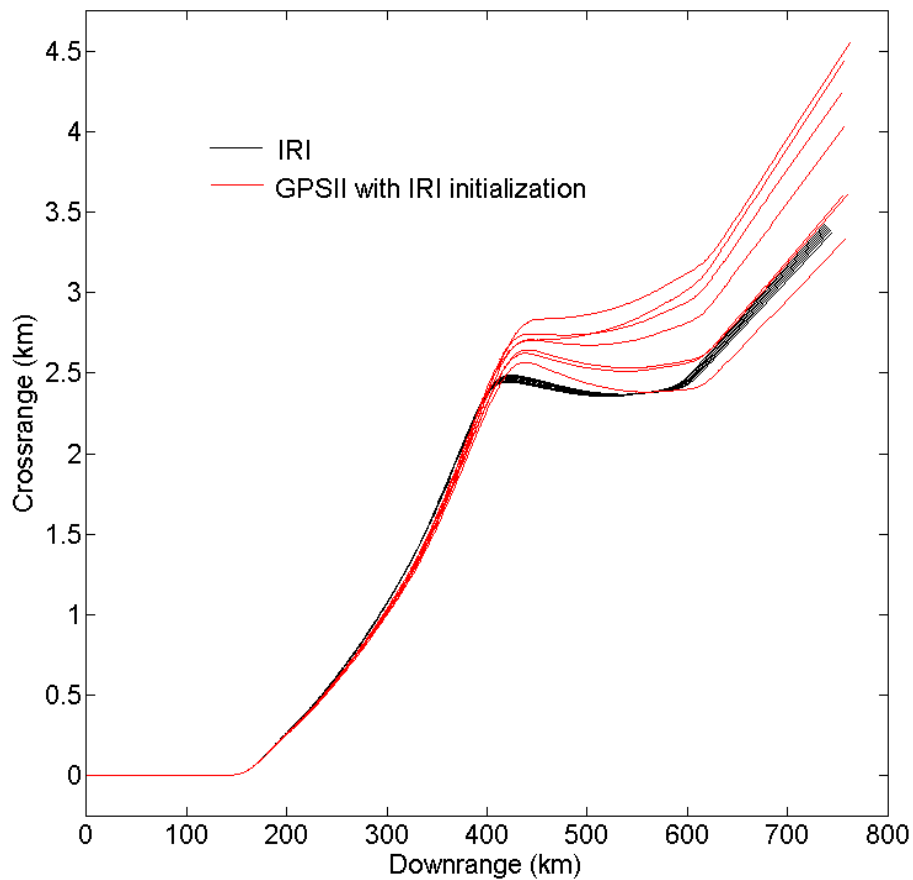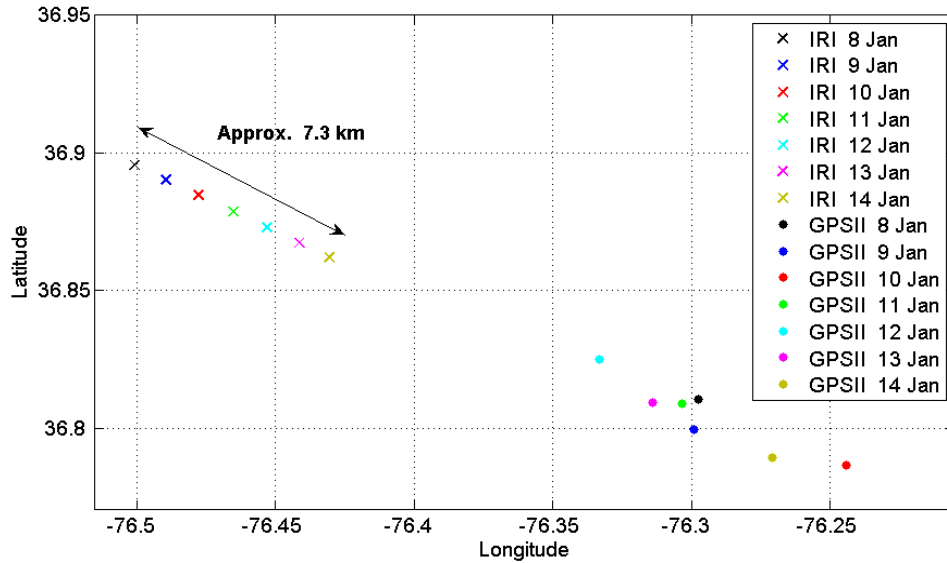

Figure 25: Receiver location (where a signal returns to the Earth's surface) for a 7 MHz signal transmitted from Wright-Patterson AFB, OH toward Norfolk, VA at local noon during the week of 8 – 14 Jan 06 (very low solar and geomagnetic activity) using various ionospheric models.

These results show that the IRI model represents the daily variability of the ionosphere as fairly steady, while the GPSII model represents the daily variability as erratic. Furthermore, this daily variability has a considerable influence on the resulting receiver location. We cannot make a firm conclusion of whether the GPSII model captures the expected daily variability without comparison to ground truth data. In other words, the model may just exhibit behavior that is characteristic of such real world variability. Also keep in mind that these results are under quiet conditions. The daily variability is even more pronounced during periods of high activity.

44

Case Study #4: Solar Flare Event

This case study completely isolates the ionosphere's response to only that of a solar flare. We examine a strong X3 solar flare that occurred on 15 July 2002 during low geomagnetic activity. The flare began at approximately 2000 UT, reached a maximum at approximately 2010 UT, and returned to background levels by 2215 UT. Refer to Table 2 for the various ionospheric indices that describe the conditions during this event. The ionosphere's characteristic response to a solar flare is an enhancement of the D and lower E regions due to an increase in x-ray and EUV absorption. Since the IRI-2001 model and PIM do not have input parameters to capture this increase in x-ray/EUV flux, our focus turns to whether the GPSII model can capture the ionosphere's response using the TEC data.

Figure 26 shows the critical frequency contours during the solar flare event using the GPSII model. Each row represents successive time steps of 2000 UT (flare beginning), 2015 UT (5 minutes after flare maximum), and 2215 UT (return to background levels). The left column is the GPSII model initialized with the IRI-2001 model, while the right column is the GPSII model initialized with PIM. The contours are very similar at the beginning of the flare. An increase in the critical frequencies at 2015 UT (directly following the flare maximum) create a ridge in the contours that stretch into Indiana, Ohio, and Michigan. The GPSII model has a more pronounced ridge when initialized with PIM, including a maximum critical frequency centered over southern Michigan. The ridge disappears by 2215 UT, returning the contours to roughly their original shape and strength prior to the flare.

45
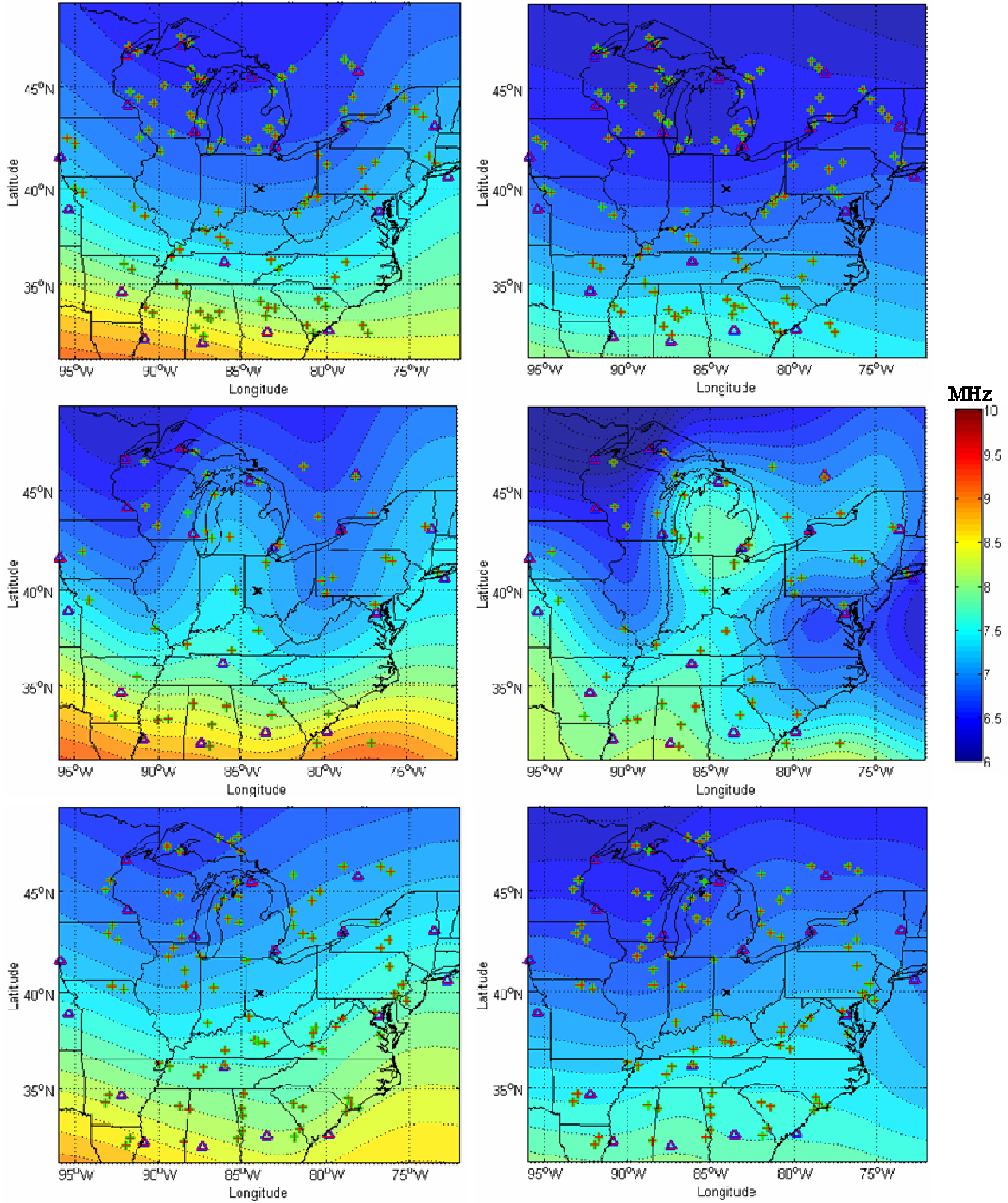
Figure 26: Critical frequency contours (MHz) during an X3 solar flare on 15 Jul 02. Left column is the GPSII model initialized with the IRI-2001 model. Right column is the GPSII model initialized with PIM. Each row represents successive time steps of before (2000 UT), during (2015 UT), and after the solar flare (2215 UT). Triangles indicate position of GPS ground receivers and crosses show position of ionospheric pierce points (at 400 km) for each satellite-receiver path.

The critical frequency contours only represent the strength of the F_2 peak. Therefore, we want to look at an entire plasma frequency profile for a location near the contour ridge. Figure 27 shows the plasma frequency profiles for WPAFB at 2000 UT and 2015 UT. As expected, the profiles of the IRI-2001 model and PIM do not change between the two times. It is interesting that PIM has a stronger F_1 region and upper E region (from 125 km to 225 km) when compared to the IRI-2001 model. The GPSII model makes the largest adjustments in plasma frequency in the upper ionosphere. This is particularly true at 2015 UT when it is initialized with PIM, resulting in an enhancement of the F_1 region as well.

As in case study #2, the GPSII model does not make any adjustments to the E layer, regardless of the initialization. We expect to see an increase in the lower E layer plasma frequencies at the time of peak x-ray and EUV fluxes during the solar flare. This ionization enhancement is due to absorption of the x-ray and EUV radiation. We can surmise that the TEC data does not assist in specifying the E layer, since the GPSII model does not show any of the expected enhancements. Remember from our earlier analysis of TEC that the contribution of the E region to vertical TEC is more or less negligible, making it exceedingly difficult to extract E region information from TEC data alone.

47
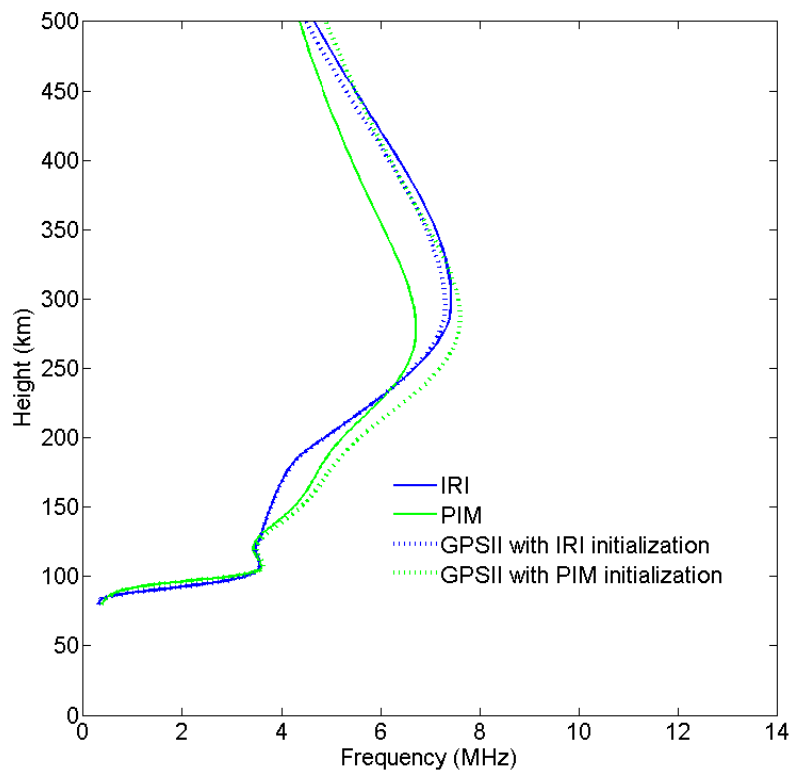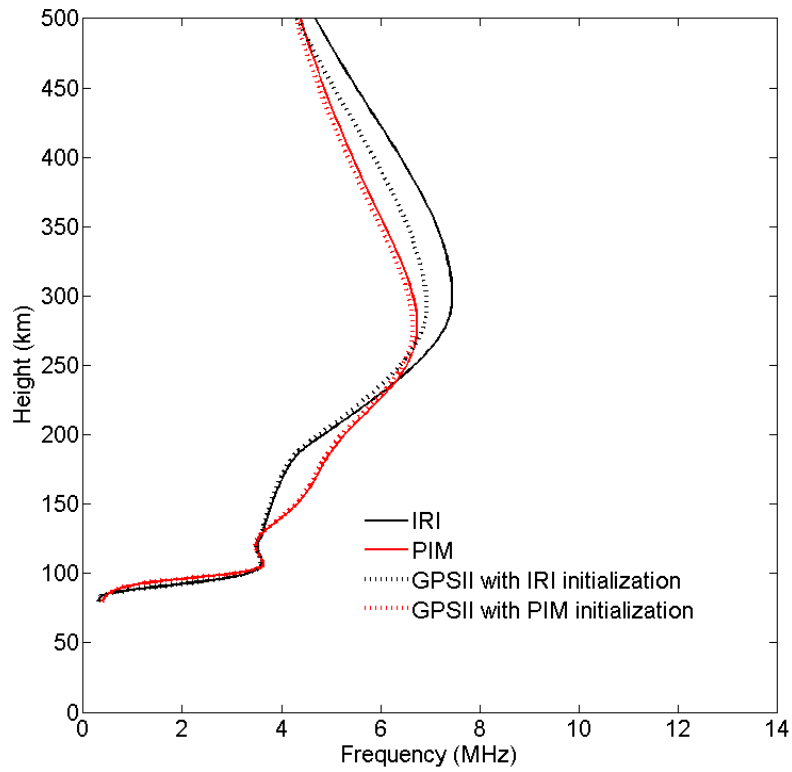
Figure 27: Plasma frequency (MHz) as a function of height (km) at Wright-Patterson AFB, OH both before (2000 UT, top) and during (2015 UT, bottom) an X3 solar flare on 15 Jul 02 using various ionospheric models.

48

Figure 28 shows the resulting propagation path (projected onto the x-z plane) of an HF signal transmitted from WPAFB toward Norfolk, VA both before and during the solar flare using the various models. Refer to Table 3 for the specific signal parameters that are used for the raytracing. PIM's stronger F_1 region and upper E region cause the signal to refract earlier in its propagation and ultimately result in longer ground ranges, seen in the red and green trajectories (essentially the E layer effect from case study #1). The GPSII model's strengthening of the F_1 region at 2015 UT also result in a longer ground range.
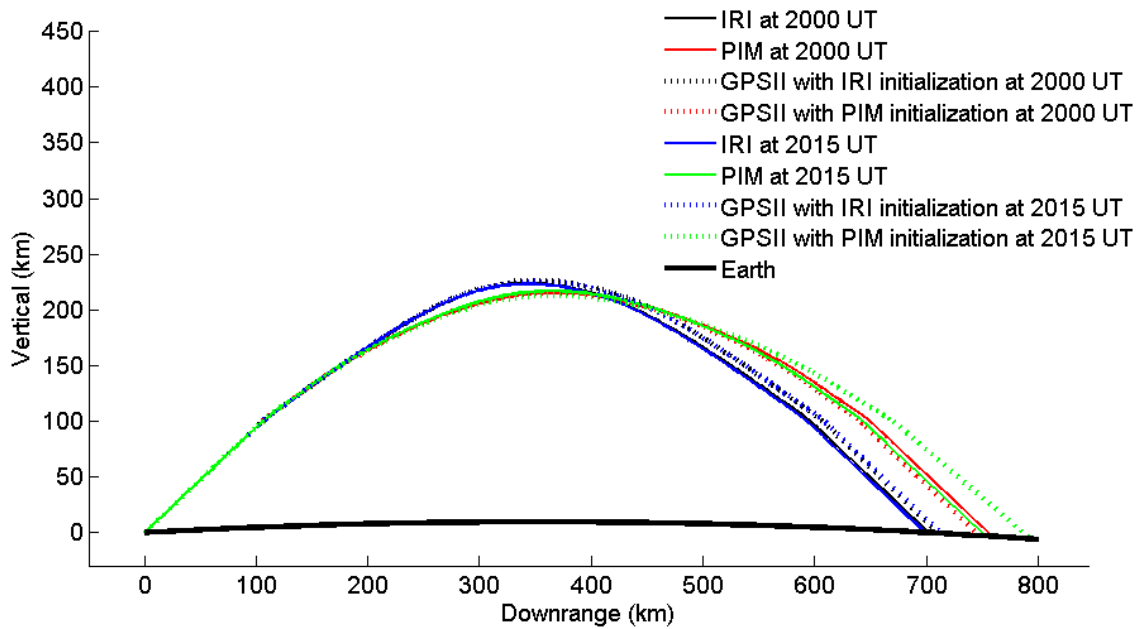
Figure 28: Propagation path projected onto the x-z plane for an 8 MHz signal transmitted from Wright-Patterson AFB, OH toward Norfolk, VA both before (2000 UT) and during (2015 UT) an X3 solar flare on 15 Jul 02 using various ionospheric models.

The corresponding receiver locations are shown in Figure 29. Remember that the GPSII model makes the largest adjustment during the flare maximum when it is initialized with PIM. This adjustment shifts the receiver location by more than 40 km.

49
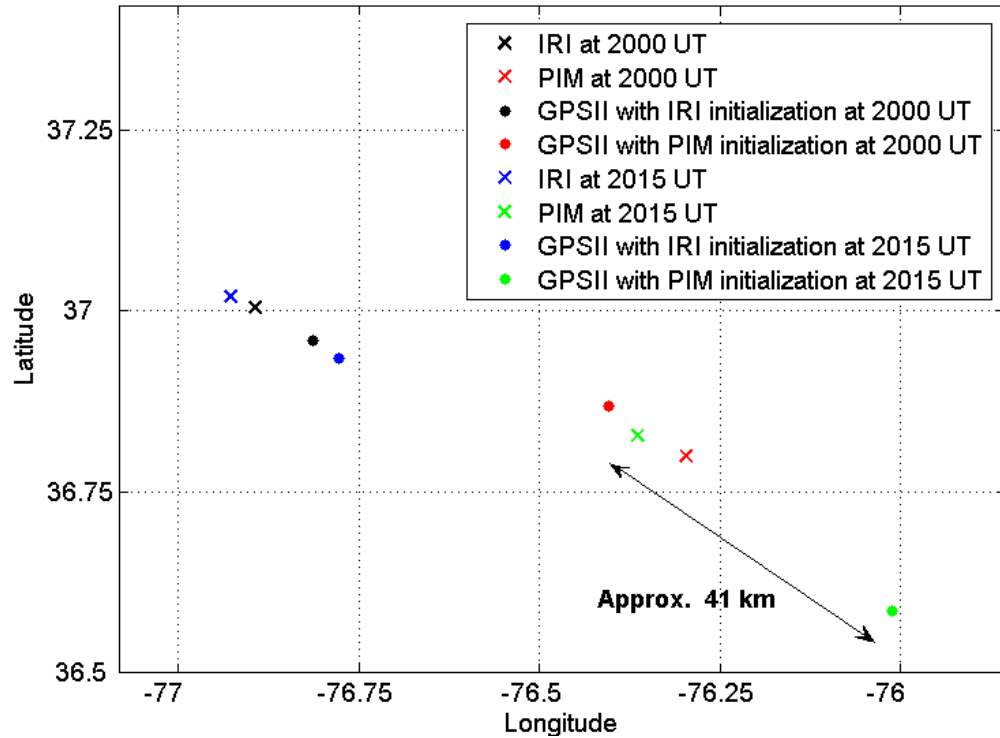
Figure 29: Receiver location (where a signal returns to the Earth's surface) for a signal transmitted from Wright-Patterson AFB, OH toward Norfolk, VA both before (2000 UT) and during (2015 UT) an X3 solar flare on 15 Jul 02 using various ionospheric models.

These results show that the IRI-2001 model and PIM can have significantly different specifications of the lower ionosphere, especially the F_1 and upper E regions. The only way to determine which model has a better specification would be to compare them to actual ionosonde data. More importantly, the GPSII model is able to capture the upper-ionospheric response to a solar flare, yet not the lower-ionospheric response. The TEC data once again does not aid in specifying the E layer. This suggests that using the GPSII model's passive technique by itself may not be sufficient, especially during solar flares when the lower E region is noticeably enhanced. Therefore, active measuring techniques may be necessary for proper specification of the E layer.

50

Case Study #5: Geomagnetic Storm Event

  This last case study isolates the ionosphere's response to only that of a geomagnetic storm. We investigate the 10th strongest geomagnetic storm of solar cycle 23 (based on maximum running 39-hour average a_p), which occurred on 27 August 1998. This storm is special because there are no significant solar flares throughout its duration (only two C-class flares). Refer to Table 2 for the various ionospheric indices that describe the conditions during this event. The ionosphere's characteristic response to a geomagnetic storm is described in Chapter II. As a reminder, the F region experiences a density enhancement during the storm's initial (or positive) phase and then depletion during the storm's main (or negative) phase. Both the IRI-2001 model and PIM have input parameters (a_p and K_p indices) that capture the geomagnetic variations, yet they only provide a limited ionospheric response when compared to the actual intensity of this strong storm. Consequently, our focus turns to whether the GPSII model can capture the ionosphere's response using the TEC data.

  Figure 30 shows the critical frequency contours during the geomagnetic storm event using the GPSII model. The left column represents the initial positive phase at 0045 UT, while the right column represents the beginning of the main negative phase at 0245 UT. The top row is the GPSII model initialized with the IRI-2001 model, while the bottom row is the GPSII model initialized with PIM. The critical frequencies approach 14 MHz for almost the entire southern region of interest during the initial phase when all 21 receivers are used in the GPSII specification. The critical frequencies decrease during the beginning of the main phase as expected, which produce a minima of approximately 4 to 5 MHz in southeastern Michigan in the GPSII model specification.

51
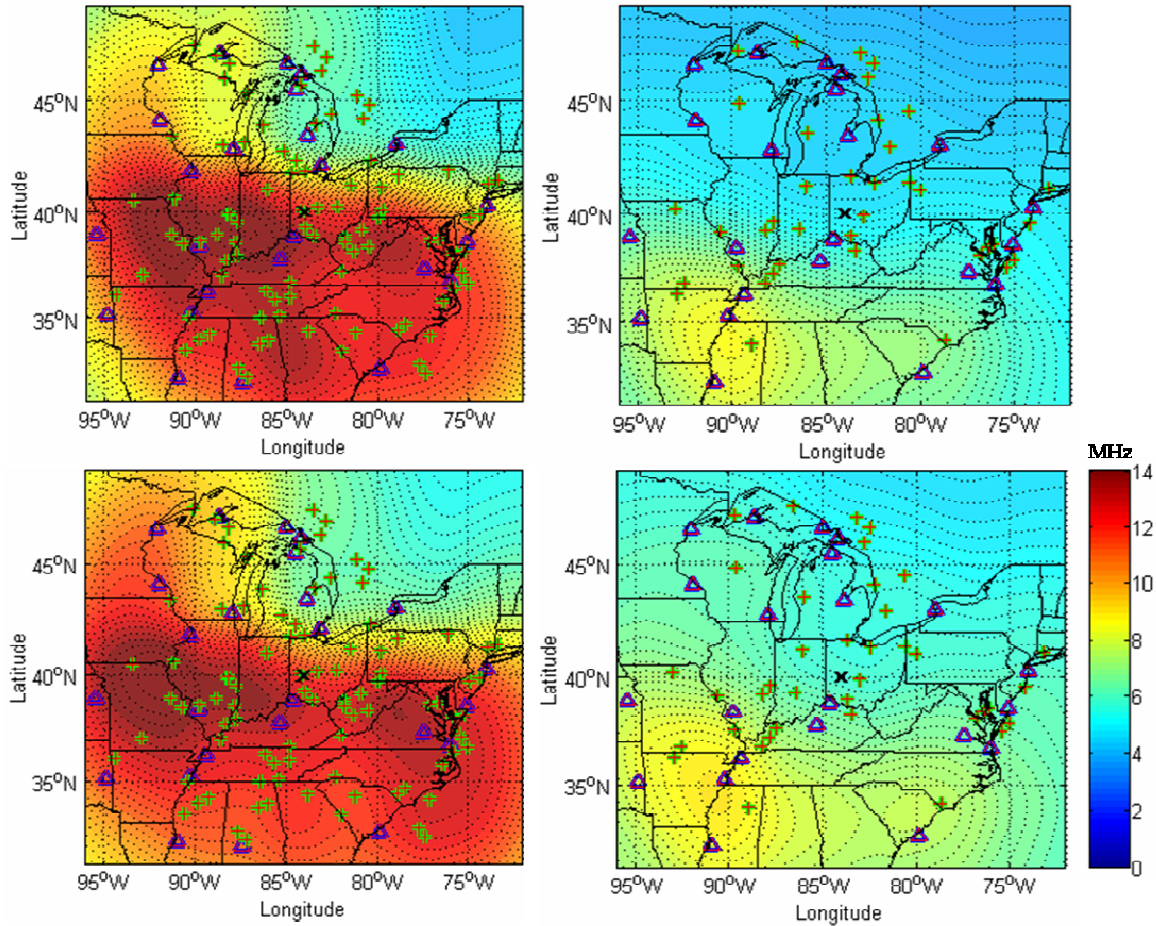
Figure 30: Critical frequency contours (MHz) during a geomagnetic storm on 27 Aug 98. Left column is during the initial positive phase (0045 UT). Right column is during the beginning of the main negative phase (0245 UT). Top row is the GPSII model initialized with the IRI-2001 model. Bottom row is the GPSII model initialized with PIM. Triangles indicate position of GPS ground receivers and crosses show position of ionospheric pierce points (at 400 km) for each satellite-receiver path.

Since the critical frequency contours only represent the strength of the F_2 peak, we want to look at an entire plasma frequency profile for a location that is near a maxima during the initial phase and near a minima during the beginning of the main phase. Figure 31 shows the plasma frequency profiles for WPAFB at 0045 UT (top) and 0245 UT (bottom). There are a few interesting profile comparisons worth noting. The profiles for both the IRI-2001 model and PIM decrease slightly above 250 km between the storm

52

phases, which is expected. The GPSII model has to make significant adjustments in plasma frequency above 250 km for the initial phase, yet makes much smaller adjustments for the main phase. PIM's lower F_1 region and upper E region (from 125 km to 200 km) strengthens slightly between the storm phases. Overall, the plasma frequencies below 225 km decrease between storm phases for each of the models. What is most interesting is that the GPSII model, as in case studies #2 and #4, does not make any adjustments to the E layer, regardless of what is used for its initialization. The TEC data once more does not aid in specifying the E layer. As we know from our previous analysis in Case Study #2, we cannot expect TEC measurements to provide much additional E region information.
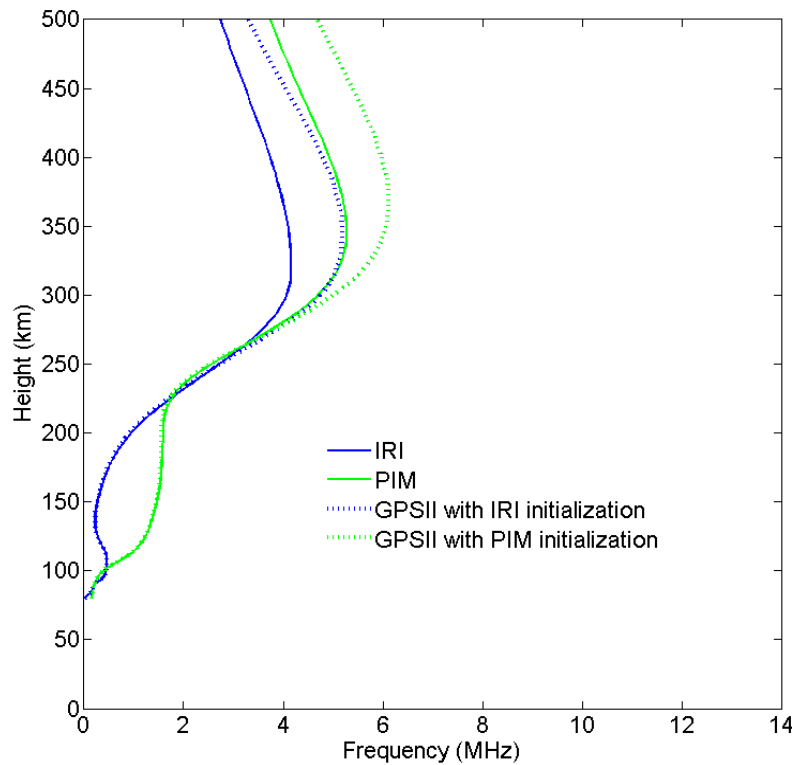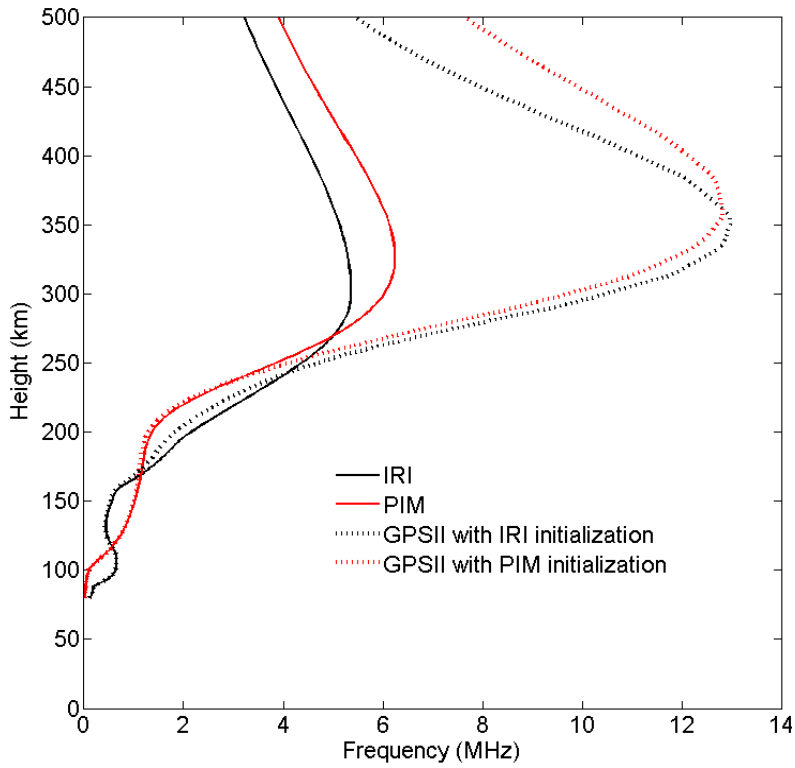
Figure 31: Plasma frequency (MHz) as a function of height (km) at the approximate apogee of a signal transmitted from Wright-Patterson AFB, OH toward Norfolk, VA for both the initial positive phase (0045 UT, top) and main negative phase (0245 UT, bottom) of a geomagnetic storm on 27 Aug 98 using various ionospheric models.

54

Figure 32 shows the resulting propagation path (projected onto the x-z plane) of an HF signal transmitted from WPAFB toward Norfolk, VA during both the initial and main phases of the geomagnetic storm using the various models. Refer to Table 3 for the specific signal parameters that are used for the raytracing. The decrease in plasma frequencies below 225 km between storm phases cause the signal's apogee height to increase for all of the models, resulting in longer ground ranges (seen in the blue and green trajectories).
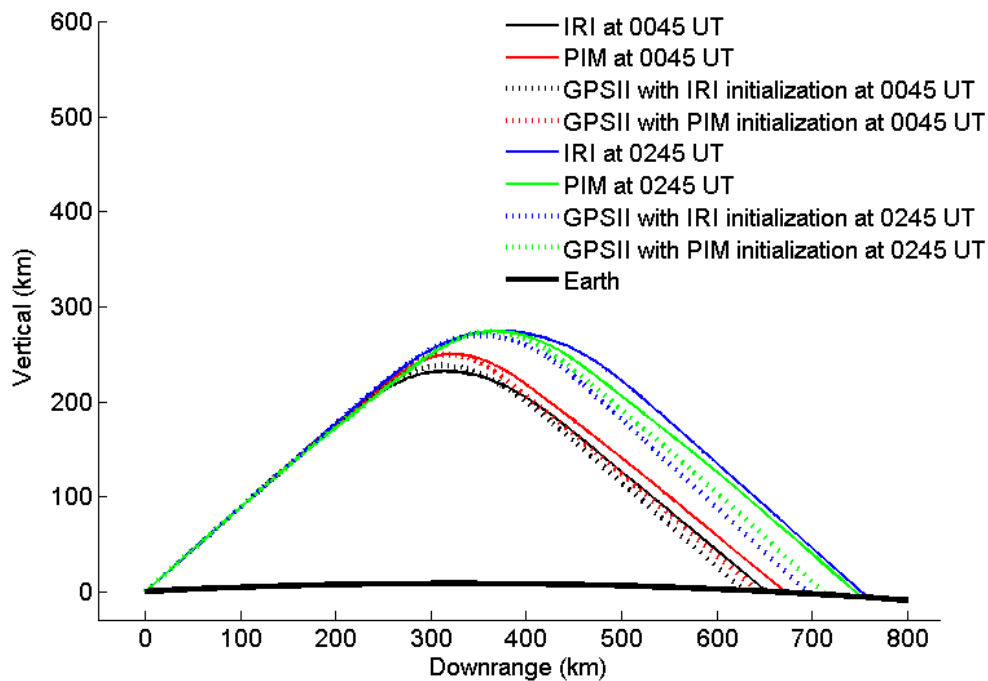
Figure 32: Propagation path projected onto the x-z plane for a 5 MHz signal transmitted from Wright-Patterson AFB, OH toward Norfolk, VA for both the initial positive phase (0045 UT) and main negative phase (0245 UT) of a geomagnetic storm on 27 Aug 98 using various ionospheric models.

The corresponding receiver locations are shown in Figure 33. The GPSII model's adjustment of PIM during the main phase has adjusted the receiver location by 36 km. In contrast, the GPSII model's adjustment of the IRI-2001 model during the main phase has adjusted the receiver location by more than 60 km.
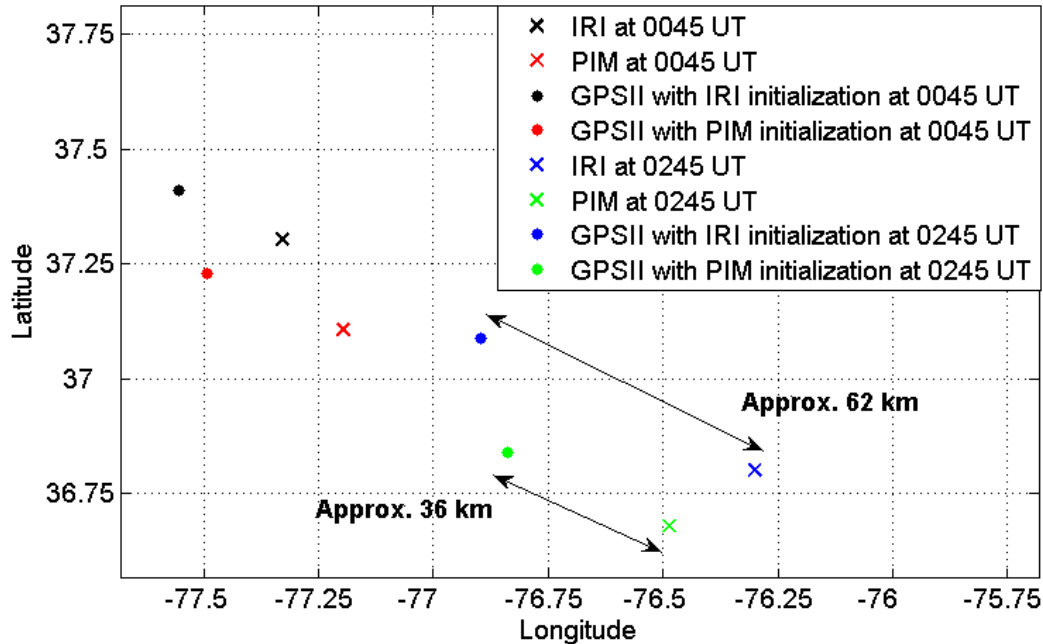
Figure 33: Receiver location (where a signal returns to the Earth's surface) for a 5 MHz signal transmitted from Wright-Patterson AFB, OH toward Norfolk, VA for both the initial positive phase (0045 UT) and main negative phase (0245 UT) of a geomagnetic storm on 27 Aug 98 using various ionospheric models.

Similar to the last case study, this case study shows that the IRI-2001 model and PIM can have significantly different specifications of the lower ionosphere, especially the lower F_1 and upper E regions. Actual ionosonde data would be needed for comparison in order to determine which model has a better specification. Of more significant importance is that the GPSII model is able to capture the upper-ionospheric response to a geomagnetic storm, yet is unable to capture the lower-ionospheric response (since TEC data provides negligible E region information). We can conclude that using the GPSII model's passive technique by itself may only be beneficial to specifying the ionosphere above the E region, especially during geomagnetic storms.

56

Conclusion

Summary

The critical national defense mission of geo-location remains highly dependent on our ability to accurately measure and predict the dynamic state of the ionosphere. The primary objective of this thesis was to assess how the IRI-2001, PIM, and GPSII ionospheric models impact HF signal raytracing during various ionospheric conditions. The secondary objective was to ascertain whether using passive techniques to model the ionosphere provide sufficient accuracy for geo-location. Three software components were used for data collection, processing, and visualization. These included the ionospheric model, the Hausman – Nickisch update of the Jones – Stephenson raytracing algorithm, and MATLAB®. Five case studies were used to explore a wide range of ionospheric conditions; including quiet, daily variability, solar flare, and geomagnetic storming.

Case study #1 showed how much the E layer by itself could significantly affect a signal's ground range and in turn impact the geo-location mission, highlighting the importance of accurately specifying the lower ionosphere. Case study #2 established a "base reference" by comparing the models at local noon on a day with quiet solar and geomagnetic conditions. It showed that the GPSII model was able to adjust for an unphysical initialization by using TEC data and, as far as quiet conditions were concerned, it showed that the GPSII model made the smallest adjustments in plasma frequency when initialized with PIM. More importantly, it provided the first evidence that the GPSII model may not be able to assist in specifying the E layer. From analyzing the definition of TEC we were able to determine that the E region's contribution to

57

vertical TEC is more or less insignificant. Consequently, it is extremely difficult to extract any reasonable E region information from TEC data alone.

The three remaining case studies focused on isolating certain ionospheric drivers. Case study #3 examined the daily variability of the ionosphere at local noon over seven consecutive days of very low solar and geomagnetic activity. The results showed that the GPSII model may be able to capture the expected daily variability of the ionosphere by using TEC data. Furthermore, we were able to see how this daily variability had a considerable affect on the resulting receiver location, which would be even more pronounced during a period of high solar and geomagnetic activity. Case studies #4 and #5 were designed to isolate the ionosphere's response to exclusively a solar flare and a geomagnetic storm. Case study #4 investigated a strong X3 solar flare that occurred on 15 July 2002 during low geomagnetic activity. Case study #5 explored an intense geomagnetic storm that occurred on 27 August 1998, in which there were no significant solar flares throughout its duration. Both case studies showed that the IRI-2001 model and PIM could have significantly different specifications of the lower ionosphere, especially the F_1 and upper E regions. Actual ionosonde data would be needed for comparison in order to determine which model had a better specification.

More significantly, the results showed that the GPSII model was able to capture the upper-ionospheric response to both the solar flare and the geomagnetic storm. Moreover, they provided further evidence that the GPSII model was not able to capture the lower-ionospheric response to these events. The TEC data simply did not assist in specifying the E layer. This suggests that using the GPSII model's passive technique by itself may only be beneficial to specifying the ionosphere above the E region, especially

58

during solar flares and geomagnetic storms. We will most likely have to rely on using active measuring techniques, such as vertical ionosondes, to accurately specify the lower ionosphere. Fortunately, the GPSII model is designed to incorporate ionosonde data. We recommend using data from ionosondes that are only located within friendly territory, so as to maintain as much passivity as possible behind enemy lines.

Future Research

The results from this thesis have generated several ideas for future research:

1) Eliminate the "bulls-eye" pattern (boundary effect) described in case study #2. This could be accomplished by increasing the latitudinal and longitudinal extent of the GPSII model's output. Note that this larger data set would require longer computational time. MATLAB® could then be used to crop the output data to a smaller region of interest, thus removing the boundary effect. Of course, the user would have to find a balance between their computational resources and the mission-dictated region of interest.

2) Determine if there are any model sensitivities when dealing with the lateral refraction of a signal, otherwise known as the signal's crossrange. In particular, examine why the crossrange of a signal can be dependent on the initialization model used. For comparison in future research, the crossrange plots not included in Chapter IV have been provided in Appendix D.

3) During the course of our research we were able to identify that a solar radio burst (concurrent with the solar flare on 15 Jul 02) caused nearly all of the GPS ground receivers in our region of interest to experience a "loss of lock" of the precision information embedded within the GPS signal. This radio burst had a peak flux of 1100 solar flux units at 1415 MHz (directly between the L1 and L2 frequency bands of the

59

GPS signal). This precision information, although still encrypted, is used by the civilian sector to improve GPS accuracy through a technique called "semicodeless tracking". This technique will be used until the next-generation GPS constellation is completed in 2012. There is a strong correlation between solar radio bursts and the loss of lock by semicodeless receivers, as reported by *Chen et al.* [2005]. Future research could include exploring the sensitivity of commercial GPS receivers to solar radio bursts that were previously considered too weak to have any effect. The MATLAB® script created for this thesis could be used to identify the number of GPS receivers affected by allegedly weak radio bursts.

4) The newest version of the GPSII model (as of 25 Jan 07) is designed to incorporate TEC data from low-Earth-orbiting (LEO) satellites. Future research could compare the GPSII model's performance when using LEO TEC data versus GPS TEC data.

5) Include ionosonde data as an input for the GPSII model. Compare its specification to those found in this thesis. Explore how changing the location of the ionosonde affects the raytracing and geo-location.

6) Finally, use ground truth data to validate the performance of the models when used for geo-location. Ground truth data would include the measured elevation and azimuth angles of frequencies received from known radio towers (beacons) as a function of time during various ionospheric conditions.

Any of these ideas, taken individually or in combination, would be suitable for future graduate research and could be completed using the same components and methodology used in this thesis. Continued research in this area will advance our ability to exploit the ionosphere and mitigate its impact on critical national defense missions.

Appendix A: Magnetoionic Splitting

The following figures were created with the raytracing algorithm. Its parameters were selected in such a way as to produce general magnetoionic splitting behavior.
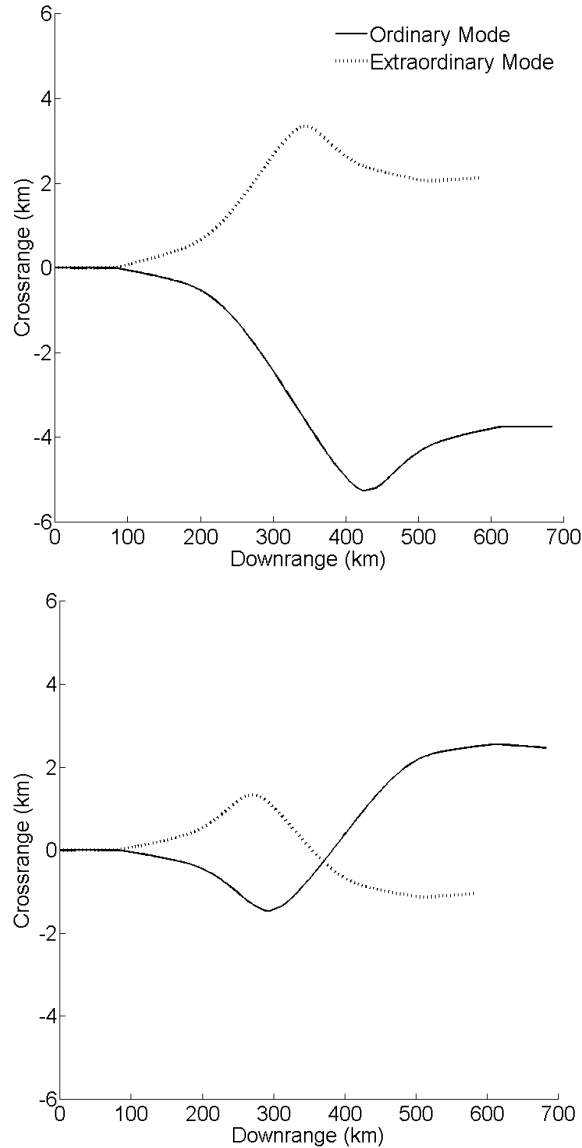
Figure 34: Magnetoionic splitting of a 10 MHz signal transmitted with elevation = 49° from Wright-Patterson AFB at local noon on the autumnal equinox during normal solar and geomagnetic activity. Shown is crossrange (km) as a function of distance downrange (km) for two transmission azimuths (top = 225°, bottom = 315°; both are _not_ in the direction of one of the four magnetic cardinal points). The signal's ordinary mode deviates toward magnetic north, while its extraordinary mode deviates toward magnetic south. Signals return to Earth in a plane parallel to the transmission plane but not necessarily coincident with it.

61
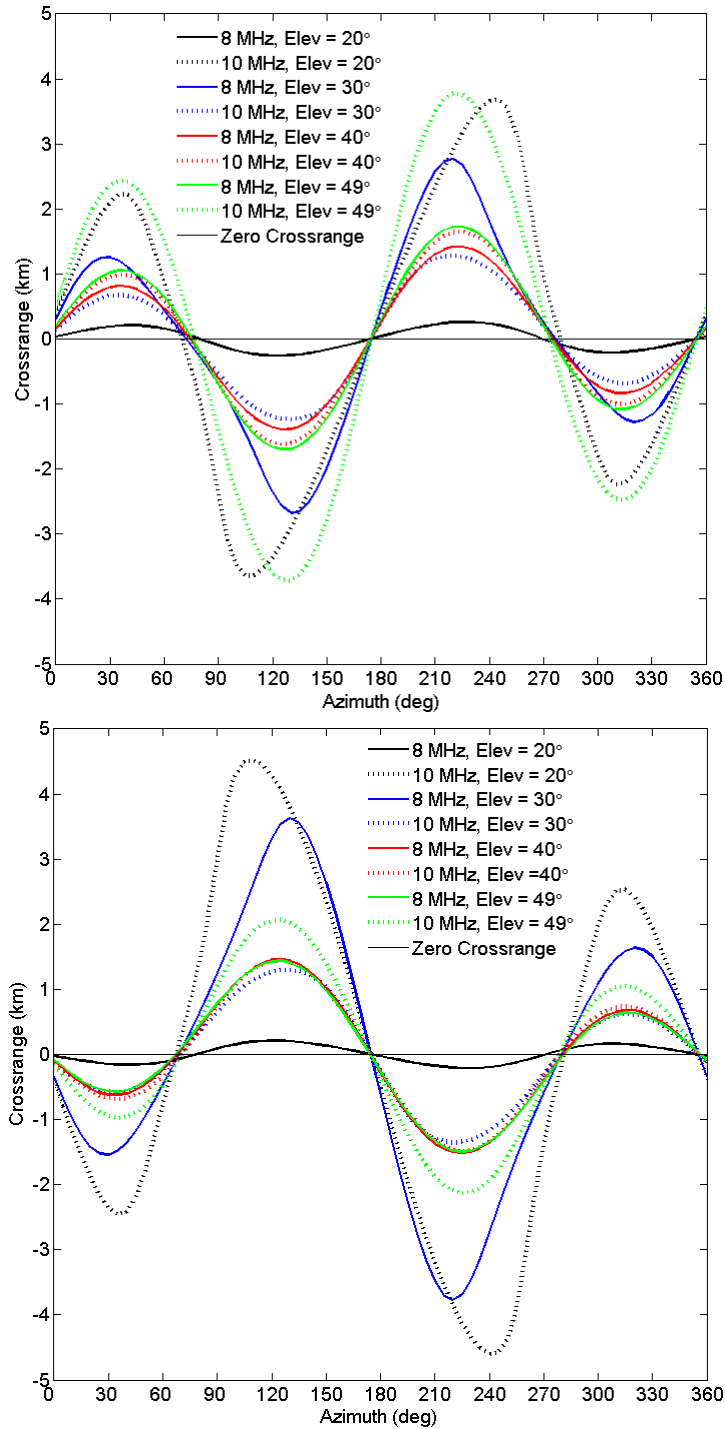
Figure 35: Final crossrange (at the point where the signal returns to Earth, in km) as a function of azimuth angle (deg) for HF signals of various frequencies and elevation angles transmitted from Wright-Patterson AFB at local noon on the autumnal equinox during normal solar and geomagnetic activity. Both the ordinary mode (top) and extraordinary mode (bottom) have zero final crossrange near the four magnetic cardinal points. Final crossrange of ordinary mode is opposite in direction to that of the extraordinary mode for all transmission azimuths.
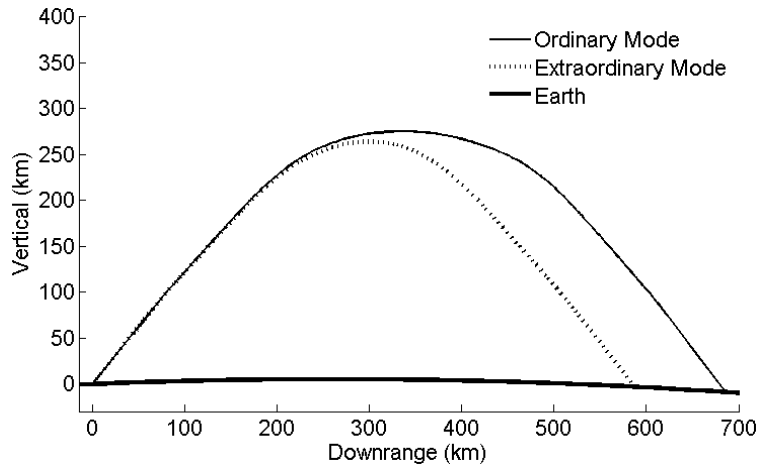
Figure 36: Magnetoionic splitting of a 10 MHz signal transmitted with elevation = 49° and azimuth = 225° from Wright-Patterson AFB at local noon on the autumnal equinox during normal solar and geomagnetic activity. Fundamentally, signal "reflection" occurs when refractive index = 0, thus for ordinary mode when $\dfrac{\omega_{plasma}^2}{\omega_{signal}^2}=1$ and for extraordinary mode when $\dfrac{\omega_{plasma}^2}{\omega_{signal}^2}=1-\dfrac{\omega_{cyclotron}}{\omega_{signal}}$. As a consequence, the extraordinary mode "reflects" earlier in its propagation, resulting in a lower apogee height and shorter ground range.
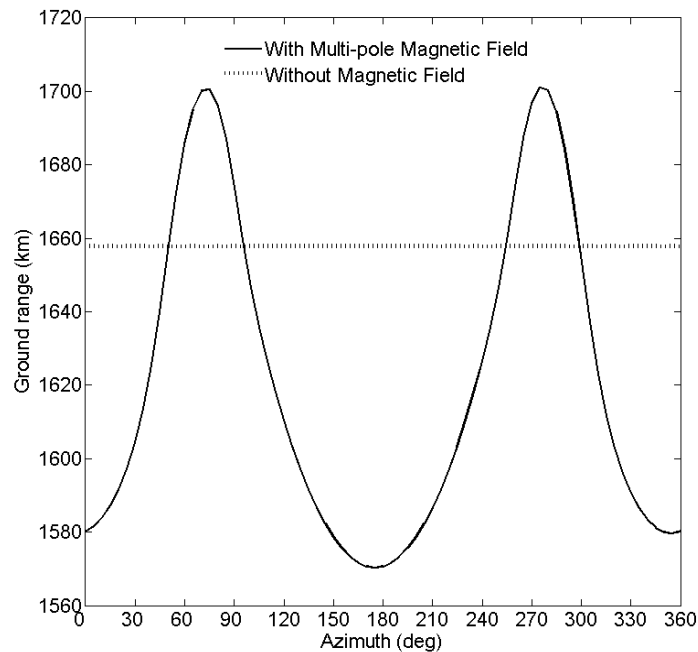
Figure 37: Ground range (km) as a function of azimuth angle (deg) for a 10 MHz signal transmitted with elevation = 20° from Wright-Patterson AFB at local noon on the autumnal equinox during normal solar and geomagnetic activity. Depending on transmission azimuth, the ordinary mode's ground range varies by as much 120 km with a magnetic field present (solid line); zero variation with no magnetic field present (dotted line).

63

Appendix B: GPSII Model Initialization File

An example of the GPSII model's initialization file, "GPS_Inv_evolve_init.txt":

```
$Initialization

!InOut_data_dir='.\GPSII_output\Case6'
name_line = '15Jul02-0000.qr          channel  1' ! Specifies the starting time of the inversion

time_interval_sec = 86400                    ! Duration of the solution interval
TimeStepMin_sec = 900!900!1800!3600        ! Temporal step of the solution
attenuation_time_sec = 3600!3600!7200!14400!        ! Time taken for a previous solution to diminish in importance by 1/e when
computing a new solution

SolarSpotIndex = 102.7                              ! User must look these values up for the specific date/time of interest
KpIndex = 1.66                                      ! User must look these values up for the specific date/time of interest

Ionosphere_Model_type = 'PIM'           !

sp3_file = 'D:\Documents and Settings\jwerner\My Documents\Raytrace\GPSII\GPS_input\2002\196\igr11751.sp3'
          !

list_file_name = 'D:\Documents and Settings\jwerner\My Documents\Raytrace\GPSII\GPS_input\2002\196\listfile_all.txt' !

RINEX_directory = 'D:\Documents and Settings\jwerner\My Documents\Raytrace\GPSII\GPS_input\2002\196\'
          !

!lat_center_degrees = 35                          ! Geographical coordinates for the central point of oblique mercator projection
!lon_center_degrees = -120             !
!skew_angle_degrees = 0                            ! Inclination of the projection
!x1min = -10.d0                        ! Modified latitude of the boundaries, counted from the center specified above
!x1max = 10.d0                         !
!x2min = -10.d0                        ! Modified longitude of the boundaries, counted from the center specified
above
!x2max = 10.d0                                     !

lat_center_degrees = 0                            ! These settings correspond to cylindrical projection: (must = 0 for
"Raytrace.exe" to work)
lon_center_degrees = 0                            ! (must = 0 for "Raytrace.exe" to work)
skew_angle_degrees = 0                            ! (must = 0 for "Raytrace.exe" to work)
x1min = 31.d0                                     ! Lower boundary of region of interest (Geographic latitude)
x1max = 49.d0                                     ! Upper boundary of region of interest (Geographic latitude)
x2min = -96.d0                                    ! Left boundary of region of interest (Geographic longitude)
x2max = -72.d0                                         ! Right boundary of region of interest (Geographic longitude)

nx1 = 37                                          ! Number of latitude grid nodes (number of divisions = nodes - 1)
nx2 = 49                                 ! Number of longitude grid nodes (number of divisions = nodes - 1)

AltTblBottom = 80.d0                              ! Specifications of the altitude grid in the output 3-D table files (km)
AltTblTop = 500.d0                      !
AltTblStep1 = 1                                   !
AltTblStep2 = 2                                   !
AltTblStep3 = 4                                   !
AltTblCross1 = 200.d0                             !
AltTblCross2 = 300.d0                             !

ElevMinDegrees = 15                     ! Minimum elevation of the satellite (deg)

IonosphereBoundaryHeightKm = 1000.0d0             ! Satellite lines of sight will be projected into this level to determine
                                                  ! whether they are inside of the area of interest

min_distance_between_rcvrs_km = 250               !

inherit_solution = .true.               !
inherit_bias_stat = .true.                        !
!inherit_solution = .false.             !
```

64

```
!inherit_bias_stat = .false.                          !

use_previously_selected_data_if_available=.true.! If true, GPSII uses the last computed solution if the run was aborted or crashed
(looks for "Selected_paths_all.bin" in working directory)

pair_relTEC_with_absTEC=.false.                       ! default is .false.

x1SmoothingHalfWidth = 6.0              ! >=0 Scale for smoothing of the background model (degrees) (set to < lat resolution
(x1max - x1min)/(nx1 - 1) for courser smoothing)
x2SmoothingHalfWidth = 6.0              ! >=0 Scale for smoothing of the background model (degrees) (set to < lon resolution
(x2max - x2min)/(nx2 - 1) for courser smoothing)


AltMin=80.d0                                          ! Specification of the computational altitude grid (km)
AltMax=20000.0d0                         !
AltStepMin=2                                  !
AltStepMax=200                           !

RxAltMin_km = -20                        ! Minimum altitude of acceptable receivers (km)
RxAltMax_km = 20                         ! Maximum altitude of acceptable receivers (km)

ReferenceLayerHeightKm = 400.0           ! Level to determine subionospheric points for plotting

Hstep = 0.05                                          ! Internal altitudinal step for kern calculation

x1_scale_deg = 6                         ! Smoothness scales
x2_scale_deg = 6                         !
alt_scale_relative = 1.0                 !

Use_Phase_data = .true.                              !
do_perform_dynamic_leveling = .true.     !

MaxIterations = 15                       !
SufficientlyManyIterations = 15          !
nTestSamples = 50                        !

iterations_to_relaxate = 0               !

regularizer_regime = 2                   ! Second order (2) or first order (1) regularizer

AbsTEC_Error = 3.6e16                    ! Will be ignored if NslidingSamples > 0

Receiver_Bias_error = 30e16             ! Initial standard deviation of the receiver bias
Transmitter_Bias_error = 15e16          ! Initial standard deviation of the transmitter bias
Receiver_Bias_Time_Const_days = 8!7              !
Transmitter_Bias_Time_Const_days = 14            !
NslidingSamples = 19                    ! For sliding estimate of the abs TEC noise
nSlidingSamplesForDifVar2 = 19          ! For phase TEC noise estimate
TEC2ndDif_est = 1.2e13                           ! 1/(m**2*sample**2)
use_sliding_averageP12 = .true.                  !
Tp_factor_base_value = 1.41d0           ! Factor to inflate noise estimates
Tp_factor_DifferentialBaseValue = 1.41           !
Tp_factor_DifferentialMaxValue = 10d0            !
TerminatorNoiseInflationMax = 2.d0               !

FitErrStartingTooBig = 5.0d3                     !
FitErrTooBig = 3.d0                               !

TECP12_noise_MaxTECU = 10.0             ! Abs TEC noise rejection threshold
dTECL12_noise_MaxTECU = 0.2             ! Relative TEC noise rejection threshold (30 s interval)

read_stored_file_names_only = .true.             !

AlphaMin = 1.d-8                                 !
AlphaMax = 1.0d8                                 !
theta = 1.2d0                                         !

AlphaPrevToAlphaLowerBound_goal = 1             ! 100
```

65

```
AlphaPrevToAlphaUpperBound_goal = 1000.0          ! Finish it
AlphaPrevEnforcementStartTStep = -10000           !

WriteTECforPlotting = .true.                       !
dTEC_threshold_TECU = 1.d0                ! Rejection threshold for testing of the first difference
                                                    ! of the phase-based TEC series per RINEX sampling period (usu
30s)
dTEC_rate_threshold_TECU = 0.1d0                  ! Rejection threshold for testing second difference
                                                    ! of the phase-based TEC series per RINEX sampling period (usu
30s)
AttenuationFactorForTderivative = 0.0d0     ! A value from 0.0 to 1.0.
                                                    ! Zero corresponds to using zero order extrapolation from the
previous
                                                    ! time step for starting solution on the current step
                                                    ! One corresponds to linear extrapolation
OptimizeAttenuation = .true.               ! <=> Select the best starting solution among solutions obtained
                                            !    with    zero    order    extrapolation    and    with
AttenuationFactorForTderivative

CenterAltitudeWithLowVariabilityKm = 285.d0       !
AltScaleLowVarability = 150.0d0                   !
RelMagnitudeOfHighVariability = 1.d0             !
diagonalProfCov = .true.                     ! .false.

$end

**********************************************************************
*************************QVI Sounders information******************
------------------------------------------------------------------------------------
SounderID,SounderLat,SounderLon(degrees
decimal),nefitFileName,ProfileFileName,ref_prof_spec,match_fof2_spec,[DeltaProfFpRel,DeltaProfFpMHz,DeltaProfHkm,[Abovek
m]]
------------------------------------------------------------------------------------
*************************End QVI Sounders*************************
**********************************************************************
'ARGUELLO' 35.6, -120.6  'nefit1.par' '06Sep04-1500-PA836_profile.tbl' 'table' 'match fof2'
'BOULDER' 40.0, -105.3  'nefit1.par' '07Aug06-1530-BC840_profile.tbl' 'table' 'match fof2' 0.03 0.10 20.0 0.0
!'VA_ROTHR' 36.4684, -76.2592  'nefit_v.par' '_qviscale_v.tbl' 'table' 'match fof2'
!Project directories:
!http://gaim.cass.usu.edu/JULY2001/GAIMHTML/page34.html
!http://www.aiub.unibe.ch/download/CODE/CODE.ACN
!http://www.ngs.noaa.gov/GPS/GPS.html
!http://140.96.176.15/GPS_WEEK/calendar.y97
```

Appendix C: Hausman – Nickisch Raytracing Algorithm Initialization File

An example of the raytracing algorithm's initialization file with extension "*.dat":

```
'AHWFNC' 'T3DLLLOG' 'NOELECT1' 'HARMONY' 'NOCOLFRZ'
!-------------------------------------------------------------------------
Testing GPSII geo-location accuracy
1    1            / 1 = ORDINARY RAY; -1 = EXTRAORDINARY RAY
4    40.0     'DEG'  / NORTH GEOGRAPHIC LATITUDE OF TRANSMITTER
5    -84.0    'DEG'  / EAST GEOGRAPHIC LONGITUDE OF TRANSMITTER
7    7.0           / INITIAL FREQUENCY (MHZ)
8    7.0           / FINAL FREQUENCY (MHZ)
9    0.            / STEP IN FREQUENCY (MHZ)
11   115.755  'DEG'  / INITIAL AZIMUTH ANGLE
12   115.755  'DEG'  / FINAL AZIMUTH ANGLE
13   0.       'DEG'  / STEP IN AZIMUTH ANGLE
15   31.166   'DEG'  / INITIAL ELEVATION ANGLE
16   31.166   'DEG'  / FINAL ELEVATION ANGLE
17   0.       'DEG'  / STEP IN ELEVATION ANGLE
19   0             / 3 = HOMER at one freq, 7 = HOMER at multiple frequencies ! change POWER FLAG = 1
20   0.            / receiver altitude (km)
22   1             / NUMBER OF HOPS
23   1.E4          / MAXIMUM NUMBER OF STEPS PER HOP
!24  78.6     'DEG'  / LATITUDE OF GEOMAGNETIC POLE (RAD)   (use this for 'DIPOLY' magnetic field)
!25  -69.8    'DEG'  / LONGITUDE OF GEOMAGNETIC POLE (RAD)  (use this for 'DIPOLY' magnetic field)
24   89.9999  'DEG'  / LATITUDE OF GEOMAGNETIC POLE (RAD)   (use this for 'HARMONY' magnetic field)
25   0.00     'DEG'  / LONGITUDE OF GEOMAGNETIC POLE (RAD)   (use this for 'HARMONY' magnetic field)
29   1             / STOPRAY (use STOPCHK routine)
30   5000.         / Stop at group path of 5000 km
42   1.E-6         / MAXIMUM RELATIVE SINGLE STEP ERROR
45   100.          / MAXIMUM INTEGRATION STEP LENGTH (KM)
57   2             / PHASE PATH        ! = 1 COMPUTE, = 2 COMPUTE AND PRINT
60   2             / PATH LENGTH       ! = 1 COMPUTE, = 2 COMPUTE AND PRINT
62   2             / TEC               ! = 1 COMPUTE, = 2 COMPUTE AND PRINT
63   1             / TEC**2            ! = 1 COMPUTE, = 2 COMPUTE AND PRINT
71   0             / NUMBER OF STEPS BETWEEN PERIODIC PRINTOUTS
72   1             / GENERATE PUNCHED OUTPUT FILE
81   5             / PLOT FLAG  (0 = no 'rayplot.bin' file; 5 = Ne grid AND rays in 'rayplot.bin'; 6 = rays in 'rayplot.bin')
83   25.      'DEG'  / LATITUDE OF BOTTOM EDGE OF PLOT  ! WHEN PLOT FLAG = 5
84   -125.    'DEG'  / LONGITUDE OF LEFT EDGE OF PLOT   ! WHEN PLOT FLAG = 5
85   50.      'DEG'  / LATITUDE OF TOP EDGE OF PLOT     ! WHEN PLOT FLAG = 5
86   -65.     'DEG'  / LONGITUDE OF RIGHT EDGE OF PLOT  ! WHEN PLOT FLAG = 5
100  1             / READ IONOSPHERIC DATA FROM TABLE FILE
221  2006.0260        / 4-DIGIT DECIMAL YEAR (fractional part = months,days) ! Use this for 'HARMONY' magnetic field)
320  0             / POWER FLAG  (1 to turn on - REQUIRED for ray homing)
!330  28.5         / Homing latitude  (note, no use of keyword 'DEG' here)
!331  -98.5        / Homing longitude  (note, no use of keyword 'DEG' here)
!332  0.01         / Homing accuracy (km)
//
!***********************************************************************
@09JAN2006_1745_GPSII_using_PIM.txt
!-------------------------------------------------------------------------
```

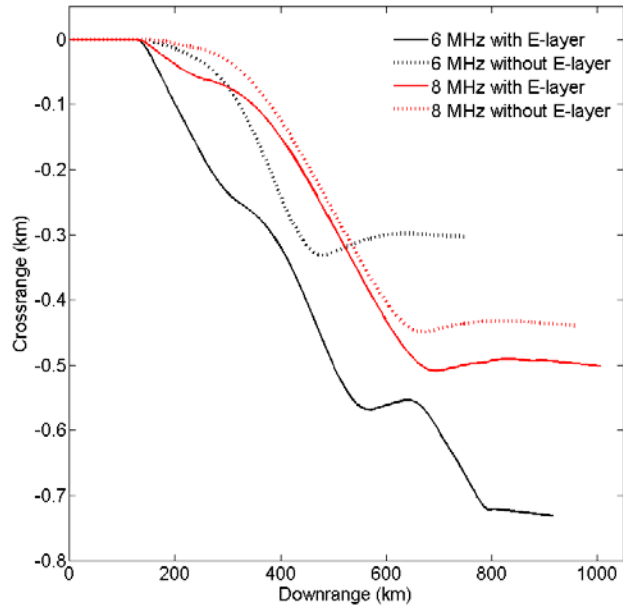**Appendix D: Crossrange Plots**

Figure 38: Crossrange (km) as a function of distance downrange (km) for a 6 MHz and 8 MHz signal transmitted with elevation = 35° and azimuth = 180° from Wright-Patterson AFB, OH at local noon on the autumnal equinox during normal solar and geomagnetic activity. Two ionospheres are used; one has an E layer (solid lines), the other does not have an E layer (dotted lines).
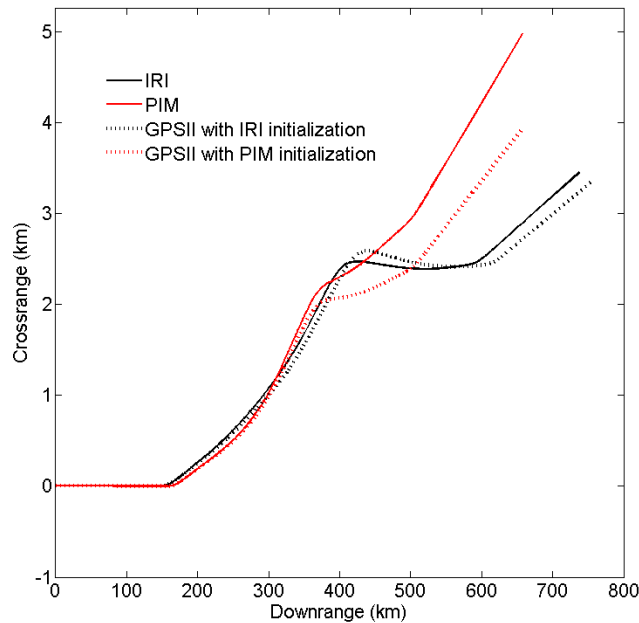

Figure 39: Crossrange (km) as a function of distance downrange (km) for a 7 MHz signal transmitted with elevation = 31.166^o from Wright-Patterson AFB, OH toward Norfolk, VA at local noon on 9 Jan 06 (quiet solar and geomagnetic conditions) using various ionospheric models.
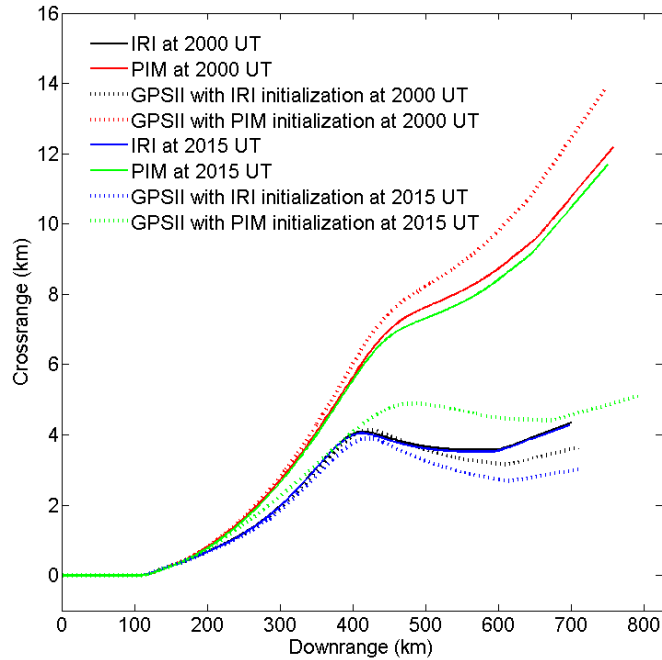
68

Figure 40: Crossrange (km) as a function of distance downrange (km) for an 8 MHz signal transmitted with elevation = 40.260^{o} from Wright-Patterson AFB, OH toward Norfolk, VA both before (2000 UT) and during (2015 UT) a solar flare on 15 Jul 02 using various ionospheric models.
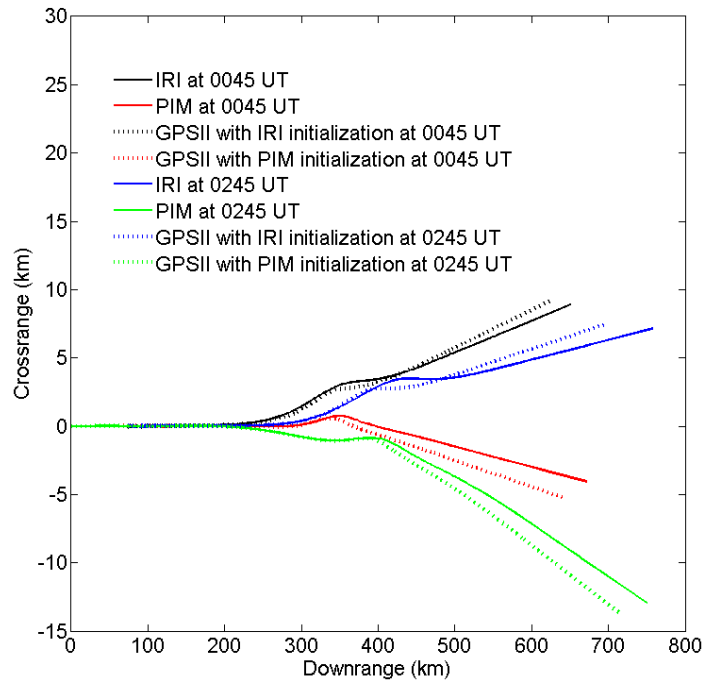

Figure 41: Crossrange (km) as a function of distance downrange (km) for a 5 MHz signal transmitted with elevation = 38.657^{o} from Wright-Patterson AFB, OH toward Norfolk, VA during the initial positive phase (0045 UT) and the beginning of the main negative phase (0245 UT) of a geomagnetic storm on 27 Aug 98 using various ionospheric models.

69

Bibliography

Aune, S. C. (2006), Comparison of ray tracing through ionospheric models, M.S. thesis, Air Force Institute of Technology, Wright-Patterson Air Force Base, Ohio.

Bilitza, D. (2001), International Reference Ionosphere 2000, *Radio Science*, *36*(2), 261-275.

Budden, K. G. (1985), *The propagation of radio waves: the theory of radio waves of low power in the ionosphere and magnetosphere*, Cambridge University Press, Cambridge, New York.

Chen, Z., Y. Gao, and Z. Liu (2005), Evaluation of solar radio bursts' effect on GPS receiver signal tracking within International GPS Service network, *Radio Science*, *40*, RS3012, doi:10.1029/2004RS003066.

Coleman, C. J. (1998), Ray tracing formulation and its application to some problems in over-the-horizon radar, *Radio Science*, *33*(4), 1187-1197.

Daniell, R. E., L. D. Brown, D. N. Anderson, M. W. Fox, P. H. Doherty, D. T. Decker, J. J. Sojka, and R. W. Schunk (1995), Parameterized ionospheric model: A global ionospheric parameterization based on first principles models, *Radio Science*, *30*(5), 1499-1510.

Davies, K. (1989), *Ionospheric radio*, Peter Peregrinus Ltd., London, U.K.

Doherty, B. D. (2004), A statistical analysis of ionospheric echoes detected by the TIGER SuperDARN radar, B.S. thesis, La Trobe University, Bundoora, Victoria

Fridman, S. V., L. J. Nickisch, M. Aiello, and M. Hausman (2006), Real-time reconstruction of the three-dimensional ionosphere using data from a network of GPS receivers, *Radio Science*, *41*, RS5S12, doi:10.1029/2005RS003341.

Hamilton, W. R., Sir (1832), Third supplement to an essay on the theory of systems of rays, *Trans. Royal Irish Acad., 17*(144), 1-144.

Hargreaves, J.K. (1992), *The solar-terrestrial environment*, Cambridge University Press, Cambridge, New York.

Haselgrove, J. (1954), Ray theory and a new method for ray tracing, *Report of Conference on the Physics of the Ionosphere*, London Physical Society, London, U.K.

70

Haselgrove, C. B., and J. Haselgrove (1960), Twisted ray paths in the ionosphere, *Proc. Phys. Soc. London*, *75*(5), 357-361.

Huang, X., and B. W. Reinisch (2006), Real-time HF ray tracing through a tilted ionosphere, *Radio Science*, *41*(8).

Jones, R. M., and J. J. Stephenson (1975), *A versatile three-dimensional ray tracing computer program for radio waves in the ionosphere*, Institute for Telecommunication Sciences, U.S. Dept. of Commerce, Office of Telecommunications, Washington.

Kelso, J. M. (1964), *Radio ray propagation in the ionosphere*, McGraw-Hill, New York.

McDonnell, M. D. (2000), A fast three-dimensional ray tracing formulation, with applications to HF communications and RADAR predictions, report, Dept. of Electrical and Electronic Engineering, The University of Adelaide, South Australia.

McNamara, L. F. (1991), *The ionosphere: communications, surveillance, and direction finding*, Krieger Publishing Company, Malabar, Florida.

Nickisch, L. J. (1988), Focusing in the stationary phase approximation, *Radio Science*, *23*(2), 171-182.

Schunk, R. W., and A. Nagy (2000), *Ionospheres: physics, plasma physics, and chemistry*, Cambridge University Press, Cambridge, New York.

Strangeways, H. J. (1997), HF transmitter location using super-resolution DF and ionospheric sounding, AGARD SPP Symposium on "Multi-Sensor Systems and Data Fusion for Telecommunication, Remote Sensing and Radar", NATO, Lisbon, Portugal.

Sturrock, P. A. (1994), *Plasma physics: an introduction to the theory of astrophysical, geophysical, and laboratory plasmas*, Cambridge University Press, Cambridge, New York.

1. REPORT DATE *(DD-MM-YYYY)* 22-03-2007	2. REPORT TYPE **Master's Thesis**	3. DATES COVERED *(From – To)* Aug 2006 – Mar 2007

4. TITLE AND SUBTITLE Assessment of the Impact of Various Ionospheric Models on High-Frequency Signal Raytracing	5a. CONTRACT NUMBER
	5b. GRANT NUMBER
	5c. PROGRAM ELEMENT NUMBER
6. AUTHOR(S) Werner, Joshua T., 1Lt, USAF	5d. PROJECT NUMBER
	5e. TASK NUMBER
	5f. WORK UNIT NUMBER

7. PERFORMING ORGANIZATION NAMES(S) AND ADDRESS(S) Air Force Institute of Technology Graduate School of Engineering and Management (AFIT/EN) 2950 Hobson Way, Building 640 WPAFB OH 45433-7765	8. PERFORMING ORGANIZATION REPORT NUMBER AFIT/GAP/ENP/07-07
9. SPONSORING/MONITORING AGENCY NAME(S) AND ADDRESS(ES)	10. SPONSOR/MONITOR'S ACRONYM(S)
	11. SPONSOR/MONITOR'S REPORT NUMBER(S)

12. DISTRIBUTION/AVAILABILITY STATEMENT

APPROVED FOR PUBLIC RELEASE; DISTRIBUTION UNLIMITED

13. SUPPLEMENTARY NOTES

14. ABSTRACT

An assessment of the impact of various ionospheric models on high-frequency (HF) signal raytracing is presented. Ionospheric refraction can strongly affect the propagation of HF signals. Consequently, Department of Defense missions such as over-the-horizon RADAR, HF communications, and geo-location all depend on an accurate specification of the ionosphere. Five case studies explore ionospheric conditions ranging from quiet conditions to solar flares and geomagnetic storms. It is shown that an E layer by itself can increase an HF signal's ground range by over 100 km, stressing the importance of accurately specifying the lower ionosphere. It is also shown that the GPSII model has the potential to capture the expected daily variability of the ionosphere by using Total Electron Content data. This daily variability can change an HF signal's ground range by as much as 5 km per day. The upper-ionospheric response to both a solar flare and a geomagnetic storm is captured by the GPSII model. In contrast, the GPSII model does not capture the lower-ionospheric response to either event. These results suggest that using the GPSII model's passive technique by itself may only be beneficial to specifying the ionosphere above the E region, especially during solar flares and geomagnetic storms.

15. SUBJECT TERMS

Ionosphere, electromagnetic wave propagation, ionospheric propagation, radio transmission, ray tracing, ionospheric model, global positioning system, solar disturbances, solar flares, magnetic storms

16. SECURITY CLASSIFICATION OF:			17. LIMITATION OF ABSTRACT	18. NUMBER OF PAGES	19a. NAME OF RESPONSIBLE PERSON Christopher G. Smithtro, Maj, USAF (ENP)
a. REPORT	b. ABSTRACT	c. THIS PAGE	UU	84	19b. TELEPHONE NUMBER *(Include area code)* (937) 255-3636, ext 4505 christopher.smithtro@afit.edu
U	U	U			

Standard Form 298 (Rev. 8-98)
Prescribed by ANSI Std. Z39-18